MOUNTAIN-PLAINS CONSORTIUM

MPC 18-362 | H. Mahmoud, M. Memari, and R. Atadero

Experimental Fatigue Assessment of CFRP-Retrofitted Reinforced Concrete Beams Subjected to Service Temperatures

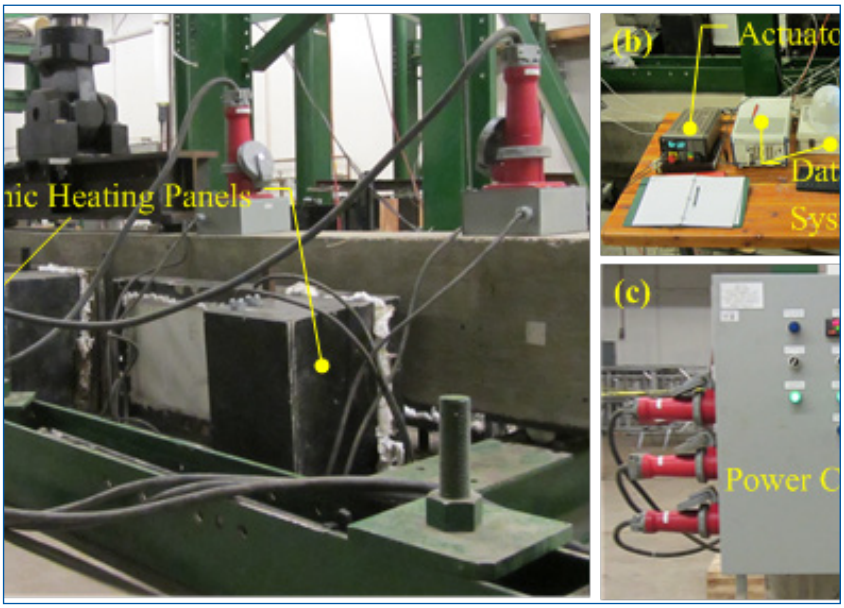

MOUNTAIN-PLAINS CONSORTIUM REGION 8

A University Transportation Center sponsored by the U.S. Department of Transportation serving the Mountain-Plains Region. Consortium members:

Colorado State University
North Dakota State University
South Dakota State University
University of Colorado Denver
University of Denver
University of Utah
Utah State University
University of Wyoming

Experimental Fatigue Assessment of CFRP-Retrofitted Reinforced Concrete Beams Subjected to Service Temperatures

Hussam Mahmoud (PI)
Mehrdad Memari
Rebecca Atadero

Department of Civil and Environmental Engineering
Colorado State University
Fort Collins, CO 80523

August 2018

Acknowledgements

The funds for this study were provided, in part, by the United States Department of Transportation to the Mountain-Plains Consortium (MPC). Matching funds were provided by Colorado State University. The data for this study was provided by Colorado State Patrol and Colorado Department of Transportation, which is greatly appreciated.

Disclaimer

ABSTRACT

The use of Carbon Fiber Reinforced Polymers (CFRP) for the repair of civil infrastructure has been on the rise. Most studies have focused on the effect of CFRP to increase the stiffness and strength of reinforced concrete beams or columns. Limited attention has been given to the effect of CFRP on mitigating fatigue crack growth in steel reinforcement. Understanding how CFRP affects fatigue crack growth in rebar is important for predicting the impact of CFRP repairs on service life extension. This paper presents the results of an experimental study on the effect of externally bonded CFRP on slowing or arresting fatigue crack growth in the steel rebar in a reinforced concrete beam subjected to cyclic loading and service temperature. Localized debonding of the CFRP was observed and is attributed to the application of service temperature. Despite the development of localized debonding, the fatigue life was extended overall in specimens repaired with CFRP systems and subjected to service temperatures in comparison to those only repaired with CFRP. Crack growth rates were used to determine material constants for the Paris Law, which describes growth of a stable fatigue crack.

TABLE OF CONTENTS

LIST OF FIGURES

LIST OF TABLES

1. LITERATURE REVIEW

1.1 Fiber reinforced polymers

Fiber reinforced polymers (FRPs) are composite materials. They are made from a combination of materials with significantly different mechanical and/or chemical properties, that when combined, create a material with properties unique from the components that comprise it. As can be assumed from the name, FRPs are comprised from two materials: a polymer resin matrix, and reinforcing fibers, as shown in Figure 1.1. The type of matrix and fiber, orientation of the fibers, and the ratio of matrix to fiber content will affect FRP properties.

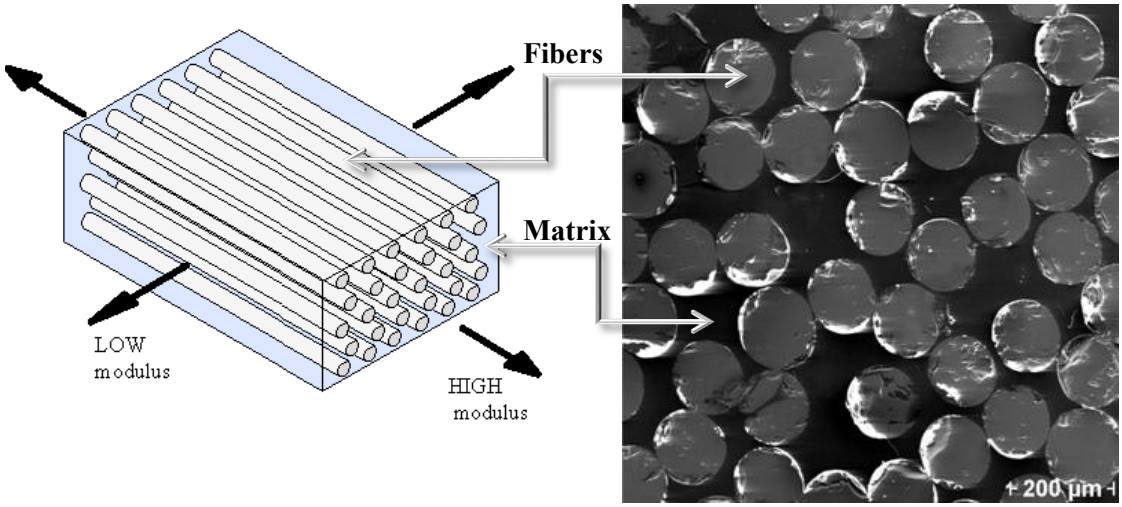

Figure 1.1 FRP composite material components (Gibson, 1994)

Fibers

While many types of fibers exist, the most common types used in structural engineering applications are Aramid fibers (Kevlar) used in AFRP, Carbon fibers used in making CFRP, and Glass fibers used in making GFRP. In the FRP fiber types, carbon has the greatest strength, typically 29,000-116,000 ksi, and it has the most resistance to fatigue failure, with an endurance limit 60–70 percent of the initial static ultimate strength (ACI Committee 440.2R, 2008).

The single fiber filaments, once produced, can be post-processed into numerous different configurations, as shown in Figure 1.2. For RC structure repairs, the most common products are near surface mount rods, prepreg strips and woven fabric sheets. The fibers in woven fabrics are typically orientated in unidirectional (0^o) or bidirectional (0^o, 90^o or 45^o, -45^o) fashion. Unidirectional fabrics are primarily used in applications where tensile forces are only present in one direction, such as flexure of a beam.

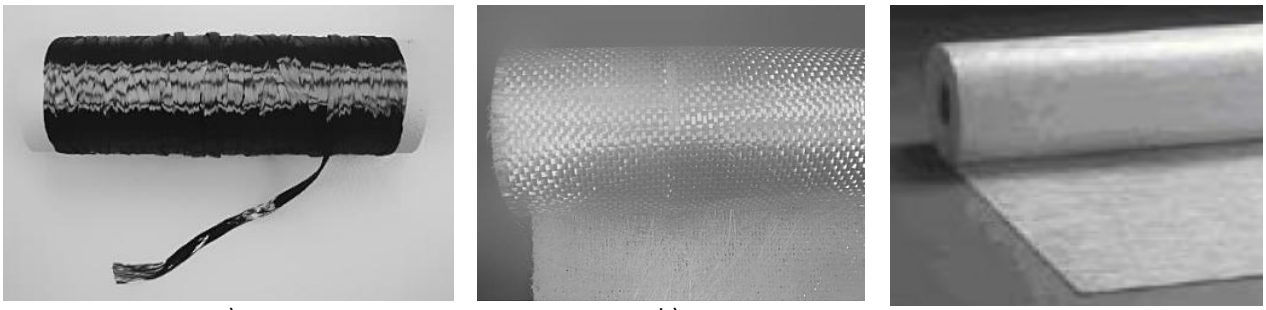

a) b) c)

Figure 1.2 Different types of FRP products: a) carbon fiber tow, b) glass fiber woven fabric, c) continuous glass filament mat (Bank, 2006)

Matrix

The matrix in FRPs is a polymer resin, which acts as the binding agent holding the fibers together, redistributing forces in the system, and protecting the fibers from mechanical and environmental damage. The difference between polymer types is based on the functional groups present in the polymer chains and how the chains interact. The two primary functional groups are thermosetting polymers and thermoplastic polymers. A limiting factor for use of many FRP systems is based on the glass transition temperature of the matrix, which is loosely defined as the temperature when a solid begins to soften and become a liquid. For thermosetting polymers, the glass transition temperature is typically around 180^{o} F. It is important for manufacturers and engineers to select and employ a matrix with a greater ultimate strain than the fibers. The correct selection ensures the brittle matrix doesn't fail (crack) before the fibers reach their maximum strength capacity (ACI Committee 440).

Typical matrix types in structural engineering applications include: unsaturated polyester, epoxy, vinyl ester, phenolic and polyurethane resins. Unsaturated polyester resins are widely used in the pultrusion process. Epoxy resins are most commonly used for retrofitting of structures because of their good adhesive properties, low shrinkage during curing, and resistance to environmental degradation. Vinyl ester resins are primarily used in the pultrusion production of FRP rebar and are a combination of unsaturated polyester and epoxy resins.

FRP Composite Properties

AFRP, CFRP and GFRP are the most widely used FRP systems because they have high ultimate strengths, low ultimate elongations, low thermal conductivity, high chemical resistance and are light weight. It is worth noting the FRP is only as strong or resilient as its components. Since FRPs are composites, they have the combined mechanical and chemical properties of the fibers and matrix. Figure 1.3 shows the tensile stress-strain relationship of a typical FRP and its components. Figure 1.4 shows the stress-strain diagrams for the different FRP types along with mild steel. It can be seen from the figure mild steel does perform better at lower strains than GFRP; however, CFRP out-performs all shown systems. It should also be noted that when unidirectional FRP systems are loaded in direct tension they remain linear-elastic (no yielding) until sudden rupture.

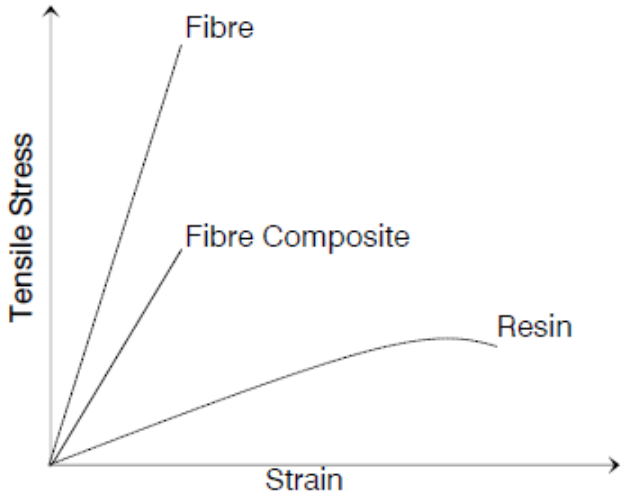

Figure 1.3 Tensile stress-strain relationship for a typical FRP and its fiber and matrix components (Badawi, 2007)

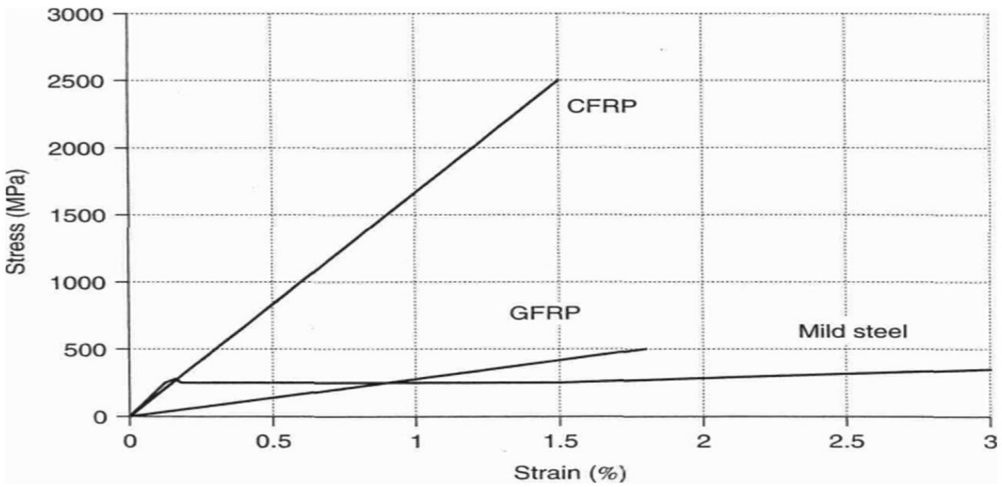

Figure 1.4 Stress-strain relationship of steel and FRP fibers (Bank, 2006)

Despite having higher tensile strength properties than steel reinforcement, the compressive strength of FRPs is quite low relative to its tensile strength. For this reason, ACI Committee 440 does not recommend the use of FRP systems in compressive strengthening applications. When FRP is applied to compressive members, it is normally used in such a way as to take advantage of its tensile strength such as confining a compression member, limiting effects like buckling, as opposed to directly resisting compression (Banks, 2006).

FRP System Applications

Structural engineers designing repairs using FRP are limited to using externally bonded FRP systems because often, only the surface is accessible. Generally, three externally bonded FRP systems are recognized: wet layup, precured, and near-surface mount (NSM) systems. Despite the nomenclature, NSM systems are still classified as an externally bonded FRP system by ACI Committee 440. Selection of

externally bonded FRP systems depends on availability of the product and trained application personal, ease and simplicity of application, and most importantly, the condition and needs of the structure.

Wet layup FRP systems are often used on structures where the application surface is relatively smooth, but has an abrupt or curved geometry, as shown in Figure 1.5. The smooth surface is a requirement of this system. It ensures proper bonding of the FRP to the structure substrate so an ideal composite action can take place. The wet layup system consists of either a unidirectional or bidirectional fabric, and a polymer resin. In the case of a wet layup system, the resin used acts not only as the composite matrix, but also as the adhesive securing the FRP to the structure. The fabric is saturated with the resin in the field by hand. It is then applied and allowed to cure on the structural surface.

Figure 1.5 CFRP fabric sheet wet layup application to girder (CPS Construction Group, 2011)

Precured FRP systems are often used when the structure's surface is smooth and flat or when it is not practical to use a wet layup. The system consists of either precured (fiber and matrix already combined) unidirectional or bidirectional laminate strips or sheets, typically delivered to the field in thin ribbon strips coiled on a roll. The system requires an adhesive for attaching it to the structure. Near surface mount FRP systems are limited to use in RC beam structures because it requires cutting a groove into the soffit of the structure, which then has a FRP rod bonded into it. The FRP bars are typically rectangular or circular in cross-section and manufactured using the pultrusion process. While additional time and effort is required for cutting the groove, increased flexural properties have been found when the NSM rods are pretensioned (Badawi, 2007).

1.2 Fatigue and Fracture Mechanics

For years, structural engineers have been aware that cyclic loading of bridges caused by passing traffic can lead to fatigue failure of structural members. Fatigue is caused by cyclic stress ranges, which are below the material's ultimate strength, causing initial microscopic flaws in the material to accumulate and grow. When these small cracks combine into large enough cracks, the cross-sectional area of the member is effectively decreased. If the crack propagates to the point where the applied load causes a stress greater than the remaining intact cross-section can endure, a sudden fracture of the member occurs. While fatigue occurs in every material subjected to cyclic loading, in this study, the focus will be on the steel reinforcing bars, which have been shown to be the limiting fatigue component in RC bridge structures (Kim and Heffernan, 2008). The steel reinforcement is considered the limiting fatigue component because concrete experiences fatigue cracking at far fewer cycles and has a lower fracture toughness (Dowling, 1999). Additionally, RC beam structures continue to perform to the desired levels despite cracking along the tension face, due to the small

amount of tensile strength supplied by the concrete in comparison to the rebar. However, when the available tensile strength provided by the rebar is removed from the equation as a result of fatigue induced fracture, the structure cannot endure with just the strength provided by the concrete.

Fatigue Failure Stages

Fatigue failures have three stages: crack initiation, crack propagation, and sudden fracture. While on the macro scale steel is considered isotropic, at a micro scale it is quite anisotropic with different crystal grains present. For ductile metals, like those composing steel reinforcing bars, the crystal grains are oriented in a fashion in which slip bands easily occur at the grain boundaries due to the applied stress. As the applied stress is cycled, these slip bands extend leading to initiation of a crack (Barsom and Rolfe, 1999). These cracks initiate more quickly at locations where stress concentrations are present. Stress concentrations can appear in many forms especially in welded components; however, for fully intact straight deformed steel reinforcing bars, stress concentrations naturally occur at the intersection of the transverse and longitudinal ribs as shown in Figure 1.6.

Figure 1.6 Fatigue crack in rebar with initiation at intersection of longitudinal and transverse ribs (Derkowski, 2006)

Once a crack is formed, it propagates perpendicular to the applied stress. In the case of tensile rebar in flexural members, the cracks propagate transversely due to the tensile forces developed. The crack will continue to propagate as long as the stress intensity factor range is above the threshold value (Barsom and Rolfe, 1999). The cracked cross-section of a piece of rebar will appear smooth due to the rubbing of the crack faces as the crack opens and closes under cyclic loading. The progress of crack propagation can also be indicated by beach marks extending away from where the crack initiated. Beach marks are semielliptical rings left in the material due to the progressing crack tip as shown in Figure 1.8.

After the crack propagates a sufficient degree, the cross-section of the component is effectively decreased to the point where the applied load induces a stress no longer below the ultimate strength of the material, and fracture occurs. The fracture stage of fatigue failure frequently occurs with no warning. In contrast to the smooth surface produced by crack propagation, the fracture surface is rough as shown in Figure 1.7.

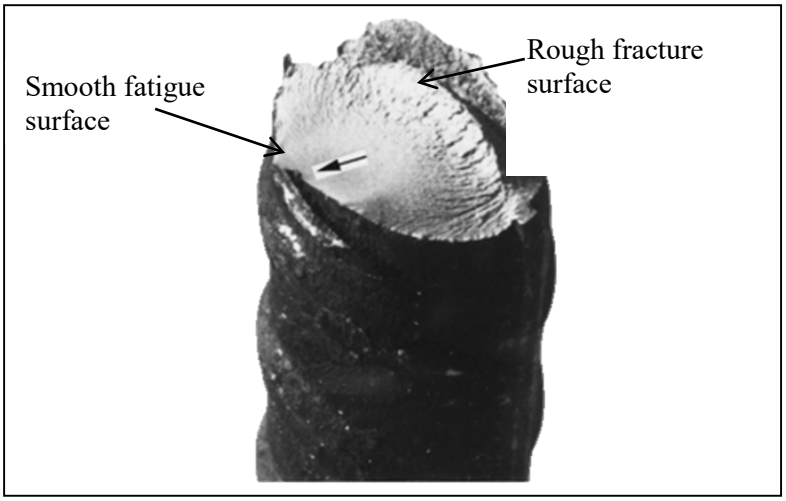

Figure 1.7 Fatigue failure of a steel reinforcing bar with crack initiating from a sharp identification mark (Zheng & Abel, 1998)

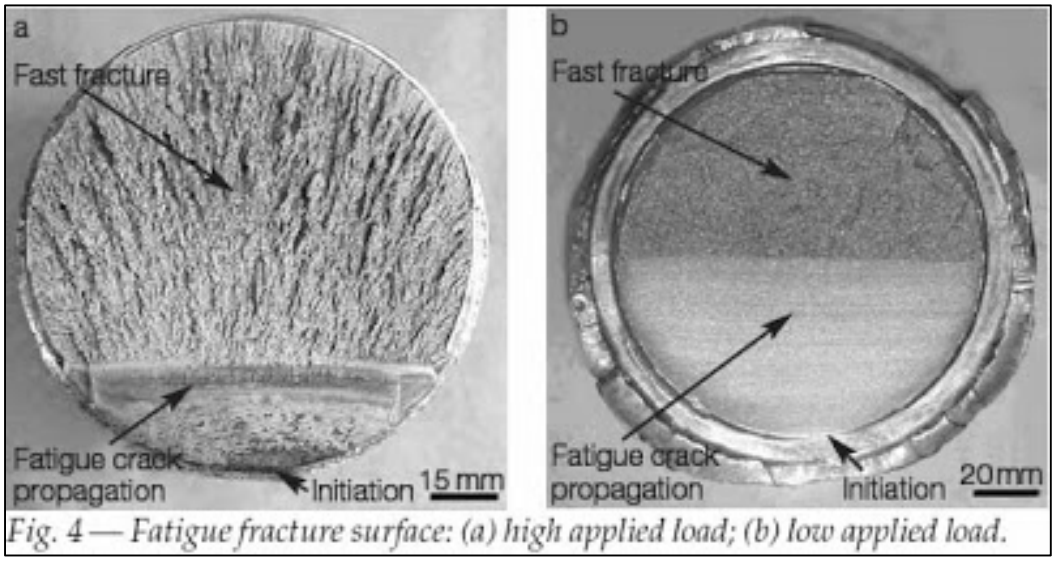

Figure 1.8 Fatigue Fracture of bolts with beach marks visible in fatigue region (Milan et al. 2004)

Linear Elastic Fracture Mechanics

Linear Elastic Fracture Mechanics (LEFM) has been recognized as the primary approach for fatigue and fracture assessment of structures (Barsom and Rolfe, 1999). The use of fracture mechanics requires determination of the material's fracture toughness, nominal stress range, flaw size and geometry. The stress field near the tip of a crack is characterized by the stress intensity factor, K_I, having units of MPa$\sqrt{m}$. This factor takes into account the nominal stress, σ, crack size, *a*, among other factors, *F*. In its most general form, the stress intensity factor under Mode I loading (opening mode) can be calculated using the following equation:

$$K_I = F\sigma\sqrt{\pi a} \tag{1.1}$$

Equations have been developed to describe the crack correction factor for many different applications. As for the case of a steel reinforcing bar with a surface flaw, the crack can be described by the equation for a round bar with a semi-circular edge crack.

$$F = \frac{\frac{1.84}{\pi}\left[\frac{\tan\left(\frac{\pi a}{4r}\right)}{\left(\frac{\pi a}{4r}\right)}\right]^{0.5}}{\cos\frac{\pi a}{4r}}\left\{0.752 + 2.02\frac{\pi a}{4r} + 0.37\left[1 - \sin\left(\frac{\pi a}{4r}\right)\right]^3\right\} \quad (1.2)$$

Where a is the flaw/crack depth and r is the radius of the bar.

The fracture toughness of a material is termed K_{IC}. The onset of fracture occurs when $K_I = K_{IC}$ where the crack size has reached its critical length and the remaining material can no longer take the applied stress. Values for K_{IC} can be determined from material tests such as the Charpy V-notch test, ASTM E23 (2007), or from assessing Equation 1.3 for the maximum stress a component will experience and the critical flaw length, a_c.

$$K_{IC} = F\sigma_{max}\sqrt{\pi a_c} \quad (1.3)$$

In fatigue, when the crack tip is cyclically stressed, this driving force parameter becomes ΔK_I, where the nominal stress term becomes the nominal stress range, $\Delta\sigma$, which is equal to the maximum stress minus the minimum stress.

$$\Delta K_I = F\Delta\sigma\sqrt{\pi a} \quad (1.4)$$

Just as a material with a flaw has a critical value for K_I, it too has a threshold value designated as ΔK_{th} for which a fatigue crack will not propagate. Conservative estimates of this threshold value can be determined from the following equation.

$$\Delta K_{th} = 7(1 - 0.85R) \;\; MPa\sqrt{m} \quad (1.5)$$

In Equation 1.5, the parameter R is the stress ratio that is equal to the minimum stress divided by the maximum stress.

Equation 1.3 can be rearranged to determine the critical crack length, a_c, if the fracture toughness is determined using a material property test, such as the aforementioned Charpy V-notch test.

$$a_c = \frac{1}{\pi}\left(\frac{K_{IC}}{F * \sigma_{max}}\right)^2 \quad (1.6)$$

In Equation 1.6, σ_{max} is the maximum nominal stress in a component.

To determine how long it will take a crack once detected, to reach its critical length, it is useful to determine the crack propagation rate. The fatigue crack growth rate is essentially the increase in crack length (a) per cycle (N) resulting in the ratio (Da/DN). However, since the change in length per cycle is small, the growth rate can be considered as the derivative, da/dN (Dowling, 1999).

In 1964, Paris proposed the Paris Law, which correlates the crack propagation rate, da/dN, and the stress intensity factor (Paris, 1964).

$$\frac{da}{dN} = C\Delta K^m \tag{1.7}$$

Where N is the number of fatigue cycles corresponding to stable crack growth, and C and m are material constants. The material constant m, is a measure of the sensitivity of the growth rate to stress and is found from the slope of the linear portion on the log-log plot. The material constant C, is then the y-intercept of the linear portion of the plot (Dowling, 1999). The relation between the crack propagation rate and the stress intensity factor range is made up of three regions: threshold region, steady growth, and unstable growth/fracture as shown in Figure 1.9. It should be noted, the Paris Law only accounts for crack growth and not initiation, which differs from the more traditional nominal stress range vs. elapsed fatigue cycles to failure, S-N curves. This will be discussed in the next section.

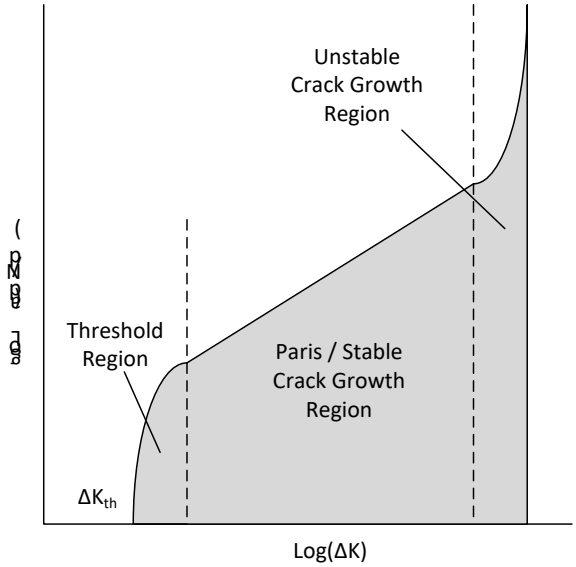

Figure 1.1 Typical crack growth rate vs. stress intensity factor range

Due to the nature of a growing crack in metallic components, the log(da/dN) versus log (ΔK) plot has a distinct S-curve shape. When a small flaw is stressed such that the stress intensity factor range is just above the threshold value, crack growth is initially quite rapid, with the curve generally having a steep slope approaching a vertical asymptote at the threshold stress intensity factor range. (Dowling, 1999). Again, this threshold value is generally the value at which cracks typically won't propagate. The next segment is the stable crack growth region described by the Paris Law. On a log-log plot, this segment should be fairly linear with the crack growth rate and stress intensity factor range increasing at the same rate. The growth rate again accelerates unstably as the stress intensity factor range becomes large, typically as the crack reaches its critical length and fracture occurs.

In addition to the crack growth rate depending on the stress intensity factor range, the growth rate also depends on the stress ratio, R ($\sigma_{min}/\sigma_{max}$), as shown in Figure 1.10. An increase in the stress ratio will cause the growth rate to increase. However, if testing conditions such as the R value, environment, and testing frequency, are held constant, the growth rate will only depend on the stress intensity factor range, DK. This is because DK accounts for the combined effects of cyclic loading, geometry, and crack length. Therefore, all da/dN vs. DK data will fall along a single line on a log-log plot as shown in Figure 1.10.

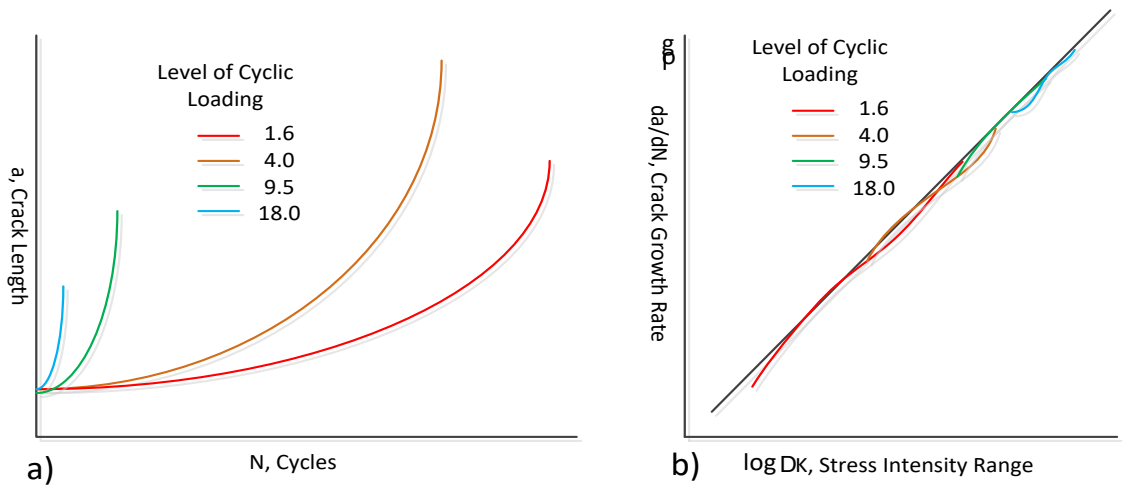

Figure 1.2 a) Crack length vs. cycles data at differing levels of cyclic load applied, b) log da/dN vs. log DK data plotted from data in plot a). (Produced from Dowling 1999)

Fatigue Life Prediction and S-N Curves

The use of the Paris Law and knowledge of factors affecting it (ΔK and R) can effectively be used to determine the fatigue life and safety inspection intervals of an in-service component. According to Dowling (1999), the first step is to test a specimen with a convenient geometry in a manner that replicates fatigue loading in the field at different stress levels, so a range of fatigue crack growth rates are acquired. The derivatives of these fatigue crack growth rates can then be plotted versus the stress intensity factor ranges on a log-log plot to create a plot similar to the one shown in Figure 1.10 b). As previously mentioned, the Paris Law material constants can be determined from this plot, which with the stress intensity factor range will produce the crack growth rate. The crack growth rate is not useful in itself without being able to determine the fatigue life of the component for which it was determined. The Paris Law Equation 1.7 can be rewritten so the number of fatigue cycles from an initial crack length to the critical crack length can be determined. To do this, an integration procedure must be used solving for N (Derkowski, 2006).

$$\int_{N_i}^{N_f} dN = N_{if} = \int_{a_i}^{a_f} \frac{da}{f(\Delta K,R)} \tag{1.8}$$

N_{if} is the number of fatigue cycles from the initial cycle to the final cycle. If it is reasonable to assume the crack shape factor, F, is constant or approximately constant throughout the fatigue life due to the crack being relatively small and the effects of R are included in the material constant C, it is possible to determine the fatigue life by substituting Equation 1.7 into Equation 1.8.

$$N_{if} = \int_{a_i}^{a_f} \frac{da}{C(\Delta K)^m} = \int_{a_i}^{a_f} \frac{da}{C\left(F\Delta\sigma\sqrt{\pi a}\right)^m} = \int_{a_i}^{a_f} \frac{1}{C\left(F\Delta\sigma\sqrt{\pi}\right)^m} \frac{da}{a^{\frac{m}{2}}}$$

$$N = \frac{2(a_c^{\frac{2-m}{2}} - a_i^{\frac{2-m}{2}})}{(2-m)C\left(F\Delta\sigma\sqrt{\pi}\right)^m} \tag{1.9}$$

Another method for predicting the fatigue life of a component is using stress range-number of cycles, S-N, curves. These curves are constructed by testing numerous specimens at different stress ranges and determining the number of cycles it takes to fail the specimen. By varying the stress amplitude, the number

of cycles to failure also varies, allowing different points on the curve to be plotted, the higher the stress amplitude the fewer cycles it takes to reach failure and vise-versa. Eventually the stress range will be so low that the stress intensity factor will be below the threshold value and the specimen will not fatigue. AASHTO (2012) has set fatigue categories, A-E, B' and E' for various components subjected to fatigue loading. Use of these categories allows an engineer to determine the lower bound fatigue life of a component if he/she knows the stress range in that component. A typical S-N plot is shown in Figure 1.11 with the AASHTO fatigue categories.

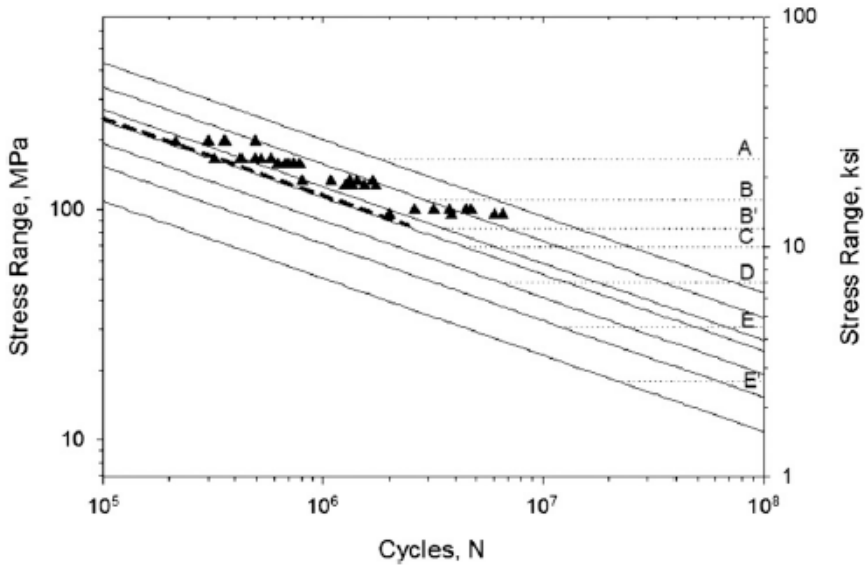

Figure 1.11 S-N test data (Fisher et al. 1974) and AASHTO fatigue design curves

S-N curves are useful due to their simplicity, but many test specimens are needed to determine a fatigue category for a new component. This becomes expensive and time-consuming since many fatigue tests reach millions of cycles. In addition, S-N curves do not take into account initial flaw sizes or pre-damage to components, limiting their use and accuracy as a fatigue life prediction method.

1.3 Existing Studies on Fatigue Performance of RC Beams Repaired with FRP

Over the past decade, research on fatigue characteristics of reinforced concrete beams strengthened with FRP has grown rapidly, with many researchers conducting experimental tests. While a large portion of the research has focused on application of externally bonded CFRP sheets or plates, other FRP types and strengthening systems, such as NSM rods, have been researched. Most papers concerned with the fatigue behavior of strengthened RC beams address at least one the following topics: 1) different CFRP strengthening configurations, 2) different anchorage systems, 3) impact of environmental conditions, or 4) fatigue life prediction models.

Review Papers

In the literature currently available, two review papers covering the fatigue performance of externally strengthened FRP beams, Kim and Heffernan (2008) and Oudah and El-Hacha (2012), exist with the purpose of informing researchers on the current state of research and the existing codes and design guidelines available to practicing engineers. These papers address fatigue characteristics of the constituent materials,

fatigue provisions in design codes such as AASHTO and ACI 440, and fatigue behavior and failure modes of strengthened beams. In addition, both papers present tables summarizing the experimental testing programs for at least a dozen papers on the subject. Oudah and El-Hacha focus more on the available fatigue life prediction models and the fatigue behavior of the materials, whereas Kim and Heffernan emphasize research on debonding and anchorage issues and design considerations.
Both papers summarize general findings from previous research on the fatigue performance of externally bonded FRP reinforced concrete beams as:

1. The addition of FRP increased the fatigue life.
2. Fracture of the tensile steel reinforcement was the initiating failure mode.
3. The critical parameter was the stress range in the reinforcing steel.
4. Debonding in the FRP-concrete interface must be addressed to achieve better performance from the repair.

Oudah and El-Hacha noted the fatigue response followed a bilinear trend as a result of reaching the full cracking stage early on during cycling. Kim and Heffernan pointed out that pre-damage to the beam had a significant effect on the fatigue behavior, therefore must be accounted for in repair designs. The authors finished their respective papers with research needs. The emphasis of the two sections was on developing design charts or procedures for practicing engineers; especially for cases where the application of such FRP systems will be for pre-damaged, retrofitted structures. The researchers found that the current design codes, AASHTO, ACI440 and ACI 215, only provide guidelines on the stress range and do not take into account other factors that can affect the fatigue life. Kim and Heffernan explicitly state "Detailed design guidelines for the fatigue limit state for reinforced concrete beams externally strengthened with FRP should be developed. Current design guidelines merely limit the strains and stresses in the FRP without providing detailed information such as the level of pre-damage in concrete or steel, environmental conditions, applied loading ranges, or expected fatigue lives." It was the goal of this study to develop a design procedure based on a fatigue limit state for the repair of pre-damaged RC bridge girders with externally bonded FRP.

FRP Strengthening Configurations

Most studies considering the fatigue performance of RC beams repaired with FRP have shown an increase in fatigue life with the addition of FRP, however, Kim and Heffernan (2008) reported the degree of fatigue life extension varies greatly, with many factors affecting the fatigue performance. Barnes and Mays (1999), Shahawy and Beitelman (1999), Mosoud et al. (2001), Papakonstantinou et al. (2001), El-Hacha et al. (2003), Aidoo et al. (2004), Heffernan and Erki (2004), Gussenhoven and Brena (2005), and Toutanji et al. (2006) showed that fatigue failure of RC beams strengthened with FRP was initiated by fatigue-fracture of the tensile reinforcing bars followed by concrete crushing, FRP delamination and/or fracture of the FRP. That so many studies have found the tensile steel reinforcement to be the limiting fatigue component, allows future studies to focus on the fatigue behavior of this element.

Gussenhoven and Breña (2005), Aidoo et al. (2006), Al-Rousan and Issa (2011), Shahawy and Beitelman (1999) and Heffernan and Erki (2004) investigated different configurations of externally bonded CFRP including number of plies, width of plies, and externally bonded prepreg strips versus hand laid-up sheets. Gussenhoven and Breña's testing was unique in the fact that the 13 tested beams were the smallest of any found in the open literature, measuring only 914mm in length. Variations in the CFRP laminate configuration and testing consisted of fatigue testing five beams strengthened with a single ply, 89mm wide sheet of M-Brace C-130, three beams which had a single-51mm wide ply, two beams which had two plies of the 51mm wide laminate, and three beams which were cyclically loaded 500,000 times in an unstrengthened state at 50 percent of the steel yield strength, then strengthened with a single layer of 51mm wide laminate and cycled until failure. Results found greater laminate thickness delayed fatigue failure of the reinforcing steel. The most astounding finding of the study was increased number of cycles to failure of beams with pre-damage. This result gives indication that the CFRP application does not extend the fatigue life of RC beams,

which is contrary to findings of every other study found. Kim et al. (2008) suggested the reason for these results was due to the same stress range applied to the steel reinforcement whether the beam was strengthened or not and due to the small size of the test specimens.

General findings from the other studies include:

- NSM exhibited greater ductility than externally bonded FRP sheets due to improved bond characteristics (Kim and Heffernan, 2008) (Badawi, 2007).
- Increased number of FRP layers and concrete contact area resulted in decrease in mid-span deflection, and increase in stiffness, ultimate load capacity and fatigue life. (Kim and Heffernan, 2008) (Aidoo et al., 2004) (Al-Rousan and Issa, 2011)
- Strengthening of the sides of beams resulted in increased effectiveness of repairs as it limited width and propagation of shear cracks and provided confining forces in the beam. (Al-Rousan and Issa, 2011) (Masoud et al., 2005) (Shahawy and Beitelman, 1999)

Corrosion Effects

Newly constructed RC structures can generally be considered quite impervious to environmental attack as the concrete provides a highly alkaline environment around the steel reinforcement which resists corroding (Masoud et al., 2005). However, after many years in service, RC structures are prone to cracking of the concrete, which can progressively get worse if the structures experience freeze-thaw cycles or over-loading caused by heavy trucks. If these cracks reach the steel reinforcement, chloride attacks from deicing agents or saltwater will eliminate the passive alkaline film and the steel will begin to corrode. The effect a corrosive environment has on a RC structure is twofold. First, the formation of rust will cause cracks to widen and concrete to spall-off, further exacerbating the problem. Second, corrosion will reduce the steel reinforcement cross-sectional area and produce corrosion pitting. In regard to fatigue, the reduction in cross-sectional area and corrosion pits can greatly decrease the fatigue life (Masoud et al., 2005). With a reduced cross-section, the remaining intact steel will experience an increased nominal stress increasing the stress intensity at any flaw, which are many due to the formation of corrosion pits. The issue then becomes can FRP repairs of these structures reduce the steel stress range such that fatigue cracking stop or at least slows such that fracture never occurs in the service life.

Masoud et al. (2005) investigated fatigue performance of RC beams that were lab-corroded and repaired with GFRP sheets. It was found that reinforcing bar pit corrosion reduced the fatigue life significantly, up to 78 percent of an uncorroded control specimen, and even when the reinforcement was corroded to a minor degree (5 percent mass loss) corrosion pits were observed to have formed, as shown in Figure 1.12. Although FRP repairs can be used to add strength to a member with a severe degree of corrosion loss, the presence of corrosion pitting must be considered when assessing at the fatigue life of the member.

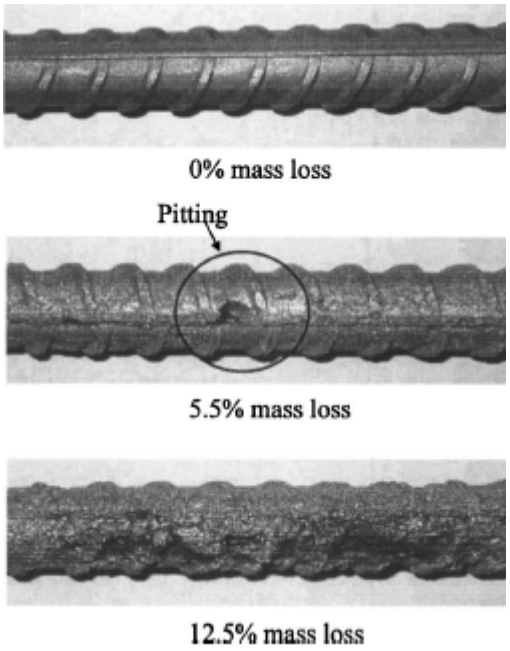

Figure 1.12 Corrosion pitting shown for varying degrees of corrosion (Masoud et al., 2005)

The study by Gonzalez et al. (1995) sought to obtain values for maximum corrosion pit depths developed in steel rebar embedded in concrete. It was proposed the maximum pit depth could be estimated using the following equation:

$$P_{max} = I_{corr} \times t \times R \tag{1.10}$$

where P_{max} is the maximum pit depth in mm, I_{corr} is the corrosion current density in μA/cm^2, t is the time in years, R is the ratio of P_{max} to P_{avg}. The authors found I_{corr} values to range from 0.001-0.005, 0.005-0.01, and >0.01 for low, medium, and high corrosion levels, respectively. R values were found to range from 4-10 with higher values correlating to more localized pitting. After six years in the Barcelona, Spain, environment, P_{max} values were found to range from 1.1–5.5mm, and R values were found to range from 2.7– 8.9.

Life Prediction Models

Studies performed by Dong et al. (2008), and Gordon and Cheng (2011) sought to develop equations and methods for characterizing fatigue life extension provided by FRP applied to RC beams. Dong et al. (2008) derived the following equation from fatigue testing 10 RC specimens strengthened with externally bonded CFRP

$$\log(N) = 6.905 - 0.0046\sigma_r \tag{1.11}$$

where N = number of cycles to failure; and σ_r = applied steel stress range (MPa). The correlation factor was 0.8808. Gordon and Cheng (2011) summarized existing S-N prediction models and derived models from available literature data. Each model's percent accuracy was determined by comparing its predicted result with the experimental results of all other studies. Although some of the S-N models provided fatigue life prediction accuracies in 10 percent of the experimental value for a particular study's data set, high inaccuracies over multiple sets of data limited any one model from providing a solid fatigue life prediction.

A 1979 study by Lovegrove, Salah El Din, and Daoud investigated the use of LEFM to predict the fatigue crack growth rate in steel reinforcing bars embedded in concrete. Similar to the current study, use of the Paris Law was highlighted. Determination of the materials constants *C* and *m* was a major focal point of the study. Difficulty of continuously measuring the fatigue crack growth throughout testing due to the limitations on having the rebar exposed is noted. To overcome this obstacle, it was proposed that two specimens are tested, each with different initial crack lengths and tested at different stress ranges. Using an integrated form of the Paris Law equation, similar to Equation 1.8, there would be two equations with only two unknowns, the material constants, since all other parameters are known from testing. Four beams were then experimentally tested f with varying initial notch depths all at the same stress range and found *m* to equal 5.3 and *C* to equal 6.3E-20. These values were then compared with values obtain from a similar steel fatigued in air which found *m* to equal 3 and *C* to equal 2.8E-13. The difference in these values suggested the fatigue crack growth rate of steel reinforcing bars embedded in concrete is lower than in air. It was noted that the stress range in the rebar could not be directly measured at the time therefore the use of conventional linear elastic equations for RC beams was used which might have had an effect on the determined values. The authors conclude the proposed technique can accurately predict the material constants of the Paris Law.

A study conducted by Rocha and Brühwiler (2012) also investigated fatigue life prediction using LEFM. The study gave background on LEFM, the Paris Law, the need equations and well-accepted values to predict the fatigue life of a RC flexural member. The authors then perform a case study on a railway bridge in Brazil to determine the fatigue life at the current service level and under increased use and loading.

The only study found in the open literature applying LEFM to predict fatigue life of RC beams repaired with FRP was performed by Derkowski in 2006. Similar to other studies which used LEFM as the bases for prediction, Derkowski also used the Paris Law to determine the number of cycles to failure of the reinforcing steel. The study was unique in several ways. First, the primary goal of the study was to determine a coefficient of FRP strip position, which when used with the Paris Law could more accurately predict the fatigue life of a reinforcing bar in the influence area of an externally bonded FRP strip. The proposed model takes into account the energy absorbed by strengthening and how this affects the stress intensity factor term in the Paris Law equation. It is the aspect of using the absorbed energy which is the second unique aspect of the study. Derkowski relates the absorbed energy to the J-integral and then the steels' modulus of elasticity to the stress intensity factor range. The proposed model was then validated with fatigue testing four RC beams with different CFRP strip configurations and compared with the experimental fatigue life. Results showed the typical increase in fatigue performance with addition of FRP, however the most important finding was the positive agreement between the predicted and experimental fatigue lives, which at the worst had a difference of 21.5 percent.

As mentioned, due to the empirical nature of S-N curves, the application of these models for predicting fatigue life of strengthened RC beams is often inaccurate due to testing and specimen variation. For that reason, the fact that the use of LEFM can take into account more of the factors that affect the fatigue life, such as pre-damage, and the promising results of recent studies using LEFM, it was determined its use in the present study was beneficial.

Effects of Service Temperatures

A prior study by Sobiek et al. (2014) showed that the addition of the FRP sheets was able to reduce the strains in the steel, and thereby extend the fatigue life of the reinforcing steel. No issues of debonding between the concrete and FRP were reported in the prior study by Sobiek et al. (2014), which insured that the FRP could effectively share in load carrying. The materials used to bond the FRP to the concrete—either the epoxy resin used to form wet-layup composites on the surface of the beam or the adhesive used for prefabricated FRP laminates—are known to be sensitive to temperature, particularly when the epoxy or adhesive is cured under ambient field conditions. Approaching the glass transition temperature of the

polymer, the epoxy will transform from a stiff, glass-like material to a rubbery material with significantly lower mechanical properties at elevated temperatures (Yu and Kodur 2010). This reduction in mechanical properties could interfere with the effective transfer of load from the RC beam to the FRP sheet, limiting the ability of the FRP to limit strains in the reinforcing steel and reducing the expected extension in fatigue life due to the addition of the FRP. In this study, the maximum applied service temperature is 41oC, well below the glass transition temperature, Tg, of the adhesive, which is 82oC according to Kodur (2010). Therefore, there is no expected effect from the applied temperature on the bonding between the concrete and the FRP. This is consistent with previous studies where it was noted that temperatures lower than 50°C have no effect on the bonding between concrete and FRP (Blontrock 2003; Wu et al. 2005; Gamage et al. 2006; Klamer et al. 2008; Cai 2008; and Leone et al. 2009). These investigations.

Other Testing Variations

Heffernan and Erki (2004), Papakonstantinou et al. (2001), Toutanji et al. (2006), Gussenhoven and Breña (2005), Aidoo et al. (2006) and Barnes and Mays (1999) considered the effect load intensity had on the fatigue performance of RC beams strengthened with FRP; either adjusting the loading as a percentage of the steel yield strength or a percentage of the static capacity of the unstrengthened beam. It was generally found that loading between 30 and 50 percent of the steel yield strength did not produce fatiguing of the specimen. For the sake of testing practicality, the stress ranges induced in the rebar of the test specimens were much higher than those that would typically be experienced in the field. It was not uncommon for the steel stress ranges in unstrengthened beams to reach 200 MPa with some specimens reaching 400 MPa. These values are 19 percent and 60 percent higher, respectively, than the 162 MPa permissible stress range recommended by AASHTO. It will be shown later in this paper that the stress ranges produced in the tensile steel reinforcement of test specimens for the current study were between 88 and 107 MPa, 21 percent and 26 percent of the yield strength of the steel reinforcement, which still produced fatigue failure of the rebar.

1.4 Existing Design Guidelines and Recommendations

Currently ACI 440.2 *Guide for the Design and Construction of Externally Bonded FRP Systems for Strengthening Concrete Structures* is the most widely used and recognized design document for FRP repairs of RC structures in the United States. The design approach taken by ACI 440.2 for serviceability of a flexural member, limits the stress in the steel reinforcement to below 80 percent of the yield strength to avoid inelastic deformations. Fatigue failure of the FRP is addressed by limiting the sustained plus cyclic stress in the different FRP types as a function of the ultimate tensile design strength. While the provision states “the possible failure modes and subsequent strains and stresses in each material should be assessed,” at no point is fatigue of the steel reinforcement considered. To address fatigue of the steel reinforcement, which has been shown to be the primary failure mode, other design codes such as AASHTO LFRD Bridge Design Specification or ACI-215 must be used.

Section 5: Concrete Structures of the AASHTO Bridge Design Specifications states the following fatigue consideration for steel rebar shall be met:

$$\gamma(\Delta f) \leq (\Delta F)_{TH} \tag{1.12}$$

where γ = the load factor for the Fatigue I load combination, Δf = the live load stress range due to the passage of the fatigue load (MPa), and ΔF_{TH} = constant-amplitude fatigue threshold which is equal to 165 - $0.33f_{min}$ for straight reinforcement, where f_{min} is the minimum live-load stress (MPa) resulting from the Fatigue I load combination, combined with the more severe stress from either the permanent loads or the permanent loads, shrinkage, and creep-induced external loads. While AASHTO does more to provide limits

on the steel reinforcement stress range, because it is for new construction, it is concerned with preventing crack initiation and does not address fatigue damage accumulation.

ACI-215 *Considerations for Design of Concrete Structures Subjected to Fatigue Loading* recommends for straight deformed steel reinforcement in non-pre-stressed members, the stress range shall not exceed the value computed from the following expression:

$$S_r = 161 - 0.33\ S_{min} \tag{1.13}$$

where S_r = stress range (MPa) and S_{min} = algebraic minimum stress (MPa). The similarity between the limits set by AASHTO and ACI-215 should be noted. While ACI-215 does discuss other variables affecting the fatigue performance such as minimum stress, bar size and type, geometry of deformations, yield strength and bending, no recommendations on fatigue life are made based on these variables.

The currently available design codes simply limit the stress range to a level below the fatigue threshold, with no consideration as to how long the FRP repair will extend the fatigue life at the current live load stress range or any other variables affecting the performance. In other words, the current design philosophy essentially recommends the engineer design an FRP repair scheme that produces an overly conservative, infinite fatigue life.

1.5 Measuring Fatigue Crack Growth

To obtain valid results of the crack growth rate in the rebar cross-section, an accurate method of measuring the crack length was needed. The trouble with measuring crack propagation in the rebar of RC structures, compared to entirely steel structures, is that rebar generally cannot be visually inspected during loading because it is embedded in concrete. Several methods were investigated based off a chart provided by Frost et al. (1974), shown in Figure 1.13 listing fatigue crack growth measurement techniques, including several non-destructive testing (NDT) methods and visual methods. While some of the measurement techniques provided by Frost were developed for crack growth measurement in steel components many appeared to be applicable to the steel in RC components.

Method	Usage	Advantages	Disadvantages
Microscopy techniques	Sheet and plate test-pieces. Photography sometimes used	Cheap. Easy installation.	Difficulty of crack tip location without stroboscopic light. Only surface measurements possible during test. Difficult to automate.
Mechanical methods	Rotating bend test pieces. Sheet, plate, and others depending on displacement gauge used	Use of compliance change which can be measured externally away from specimen.	Restricted to tests where compliance calibration (relationship between specimen stiffness and crack length) is known.
Acoustic methods	Applicable to most types of test-piece	Very small probe required, can be mounted easily; useful in low- and high-temperature tests.	Errors due to background noise and calibration is difficult
Electrical techniques	Continuity gauges usually used on sheet and plate samples, could be used for surface measurements on other test-pieces	Electrical signal gives easy automation.	Difficulty of connecting wire and foil gauges. Gauges must break when crack passes. Only surface measurement.
Eddy currents	Used on surface crack monitoring of sheet test-pieces; others should be possible.	Easily adapted to automatic process. Small probe which is not in contact with test-piece.	Not yet used on thicker samples, may only be useful for surface measurement. Expensive.
Electrical resistance or potential measurement	Used on sheet and plate test-pieces	Easily adapted to automatic process. Only four leads attached to specimen, therefore ideally suited for high- or low-temperature tests	Problems of insulating the test-piece. Initial calibration problem thought to be overcome.
Ultrasonics	Ideally suited to compact fracture toughness test-pieces. (Fig. 5.2).	Easily adapted to automatic process. Internal measurement of crack front.	Expensive compared to other techniques. Measurements restricted to thicker type test-pieces.

Figure 1.13 Fatigue crack growth measurement techniques (Frost et al, 1974)

NDT methods for determining the fatigue crack growth rate were initially investigated. They would allow crack measurement in an intact RC beam, where direct access to the rebar at the crack location was not possible. NDT is any technique used to evaluate a material, component or system without causing damage. Several types of NDT commonly used in structural engineering applications include acoustic emission, electro-magnetic, radiography, ultrasonic, x-ray, impact echo, and electric potential. The problem with many of these methods is that they are limited to determining the location of flaws, voids, joints, and depth and placement of rebar and conduit and are unable to determine propagation of cracks with any certainty. Despite these limitations, engineers have been innovative in the use of some of these methods and eventually have determined the size, location and growth rates of fatigue cracks in concrete. While some of these methods are unrealistic for field use, the goal of this study was not to investigate applicability of such methods for field use, but to study how fatigue crack growth rates are affected by the application of CFRP to RC structures.

Acoustic Emission

One NDT method shown to be effective in evaluating fatigue crack growth rates in two-dimensional members is acoustic emission (AE). The technique involves sensing transient elastic waves generated when energy is rapidly released from a localized source, often a flaw or void, as they propagate through the solid material. The AE method is unique in the way the measured energy signal is supplied from the test material, through the stressing of a flaw, and not from an external transducer.

With technological advances in computing and signal processing, the AE method has become commercially available and capable of detecting the small changes in the stress wave as a result of a growing crack. Shah and Kishen (2012) have shown with proper calibration this method can determine the location of a crack in a material and, with continued monitoring, determine the crack propagation characteristics under fatigue loading. However, the problem with translating this method to the current study is that the interest of this study is in determining the crack growth rate in the reinforcing bars, which are essentially one-dimensional. The AE method would only identify the location of cracking and not the growth of a fatigue crack because the AE sensors would only have access to the rebar, which would have to be extended out the ends of the beam. Along with a substantial cost and the need for a skilled technician, a more direct and economical method was pursued.

Electric Potential Drop

Another method suggested by Frost for studying the fatigue crack growth characteristics was electric potential drop. This method was initially investigated because it would need physical access to rebar just as the AE method did. The electric potential drop method involves measuring the drop in electric potential energy as the electric resistance of the material increases between the points of measurement.

In general, there are two categories of the electric potential drop method: 1) the alternating current technique (ACPD) and 2) the direct current technique (DCPD) (Nordtest Method, 1988). In the ACPD technique, an alternating current is passed through the metal, where most of the current density is carried only in a thin layer on the metal's surface due to the skin effect. To determine crack depth, the voltage must be measured, using potential electrodes, across the crack mouth distance before and during the presence of the crack. The crack depth can then be measured by the following expression:

$$d = \left(\frac{V_c}{V_o} - 1\right) * \left(\frac{S}{2}\right) \tag{1.14}$$

where

V_o = measured voltage between the electrodes when no crack is present
V_c = measured voltage between the electrodes with a crack present
s = distance between potential electrodes

Essentially, the ACPD technique involves measuring an increasing current path around the crack tip and relating that increased path with a progressing crack.

The DCPD technique involves passing a direct current through the metal, where the current flows through the entire cross-section, and measuring the voltage across a distance between the applied current. Using Ohm's law, the measured voltage will be given by the expression:

$$V = IR = I\left(\frac{\rho S}{A}\right) \tag{1.13}$$

where

V = measured voltage
I = applied current
R = electrical resistance
r = material resistivity
s = distance between potential electrodes
A = cross-sectional area

From this expression it can be seen that as a crack grows, the cross-sectional area decreases resulting in an increased resistance. If the current is kept constant, the measured voltage must also increase at the same rate as the resistance, allowing an equation for crack depth as a function of voltage to be derived.

The electric potential drop methods have some limitations eventually determined to be too large to work in the current study. The ACPD method requires the potential electrodes to be placed close to the crack mouth for the small changes in the current path to be measured. The DCPD method is largely dependent on the resistivity value of steel, which has a value varying from $1.43\text{-}1.71*10^{-7}$ Wm making the measured voltages very small. The problem with very small voltage readings is that the equipment required to measure the slight variation due to crack growth is very expensive. Additionally, due to the interlocking between the concrete and the reinforcing steel in RC structures, the crack mouth is restricted from opening as far. This restricted movement allows sustained contact between the crack faces, resulting in continued current flow despite the crack tip having passed this region. The increased area for current flow, regardless of electric potential drop technique, results in discrepancies in the measured voltage and therefore crack length.

Microscopy

The feasibility, physically and economically, of other NDT methods led to the investigation of visual inspection of the fatigue cracks. Instrumentation for visual inspection of fatigue cracks is typically some sort of microscope due to the relatively small size of fatigue crack in steel rebar. The use of microscopy relied on whether visual inspection of the crack was possible. The tensile rebar in RC flexural members are embedded in concrete so the tensile stresses can be transferred from the concrete, which is weak in tension, to the rebar which are strong in tension. Additionally, as mentioned before, the concrete cover provides protection of the rebar from external environmental attacks. However, in the current study, rebar protection wasn't needed as the beams would be tested relatively quickly after fabrication. Furthermore, to keep the fatigue test of each beam to a reasonable timeframe a relatively high stress loading would need to be applied to the beam. As discussed in further detail in the methodology section of this paper, the loading was calculated to produce an applied moment greater than the cracking moment of the beam, meaning the beam would have flexural crack up to the neutral axis of the beam. Because the concrete below the neutral axis was cracked it would hardly provide any tensile strength, therefore it was hypothesized a small portion of concrete could be removed exposing the rebar for visual inspection via a microscope. A digital microscope was used for practical purposes because it, with the accompanying software, could measure the crack length directly from the digital photos. To validate the prediction that removal of a small portion of the concrete would have minimal effect on the overall structural performance of the beam and fatigue crack growth rate a small-scale test was performed, and one of the full-scale test beams was fabricated without a void and compared to two identical beams with voids.

1.6 Extension of Previous Work and Significance of Present Research

In Sobieck et al. (2014), experimental evaluation of the fatigue performance of RC beams strengthened with different externally bonded carbon fiber reinforced polymer (CFRP) systems was conducted. Seven specimens were fabricated; three had no CFRP while the remaining four had one of two CFRP systems - Tyfo SCH-41 Sheet or Tyfo UC Strip Sheet. The study was conducted under room temperature and results showed an extended fatigue life and a slowed crack growth rate in specimens repaired with the CFRP systems. The study conducted by Sobieck et.al. (2014) made a unique contribution in that most prior research on the effect of externally bonded FRP on fatigue performance focused on developing models related to crack initiation, whereas Sobieck et. al. (2014) studied the propagation phase of fatigue life. The current study aims to extend previously conducted work on crack propagation while incorporating the effect of service temperature on fatigue crack growth in the rebar. It is hypothized that the difference in the coefficient of thermal expansion between the steel and concrete would result in compressive loads being applied to the steel rebar as it tries to expand faster than the concrete, which promotes crack closure, resulting in extension in fatigue life. The tests conducted in this study use the Tyfo SCH-41 sheet. In addition, results of the tests performed with no CFRP and with Tyfo SCH-41 sheet in Sobieck et al. (2014) are utilized used in this study for the sake of comparison.

2. METHODOLOGY

2.1 Small-Scale Testing

As described in section 2.5, a visual inspection of the rebar was determined to be the most economical and direct method for measurement of the fatigue crack growth rate. The direct access to the rebar also reduces uncertainty in results that may be present with other NDE techniques. To validate the prediction that removal of a small portion of the concrete would have minimal effect on the overall structural performance of the beam and fatigue crack growth rate a small-scale test was performed. The rational for the test was that if the small-scale beams with and without rebar access holes have similar performance, then the access holes are not significantly affecting beam performance. Furthermore, performance in the actual test specimens should also be unaffected by the access holes, since the removed concrete makes up a greater portion of the cross-section in the small-scale beams.

2.1.1 Manufacturing and dimensions

Three small-scale beams were constructed, each having a span of 864mm, depth of 89mm, and width of 89mm, as shown in Figure 2.1. Steel reinforcement of each beam consisted of a single 10mm, Grade 60 (420 MPa), black bar as the tensile reinforcement and shear stirrups bent from smooth steel bar with nominal area of 40.65mm2. The tensile reinforcement was placed at a depth of 70mm below the compression face of the beam. During fabrication of the stirrups a surface roughness was applied to achieve interlocking between the concrete and stirrup. The stirrups were tied to the tensile rebar in the shear zone of the beams with 50mm spacing between them. Two of the beams had cylindrical sections of the concrete removed, by placing foam tubing in the forms before concrete placement as shown in Figure 2-3. The missing concrete section measured 38mm deep and traversed the width of the beam. Quickrete high early strength sack concrete, which is rated to achieve a 27.6 MPa compressive strength at 28-days of curing, was also used. A concrete vibrator was used while placing concrete to reduce air voids in the beams. For further identification of each beam, the following designations were used: Beam 1 was fabricated with no void in the concrete and had three strain gages, Beam 2 was identical to Beam 1 but with a void, and Beam 3 was identical to Beam 2 but only had the single strain gage.

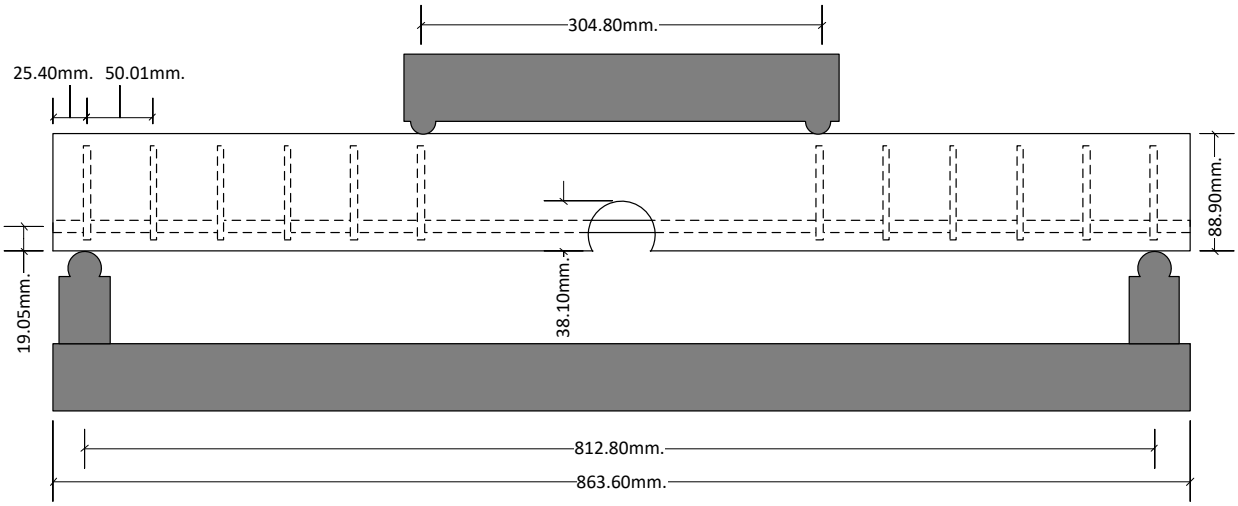

Figure 2.1 Small-scale test beam shown with rebar access hole, reinforcement detail, and support and loading points

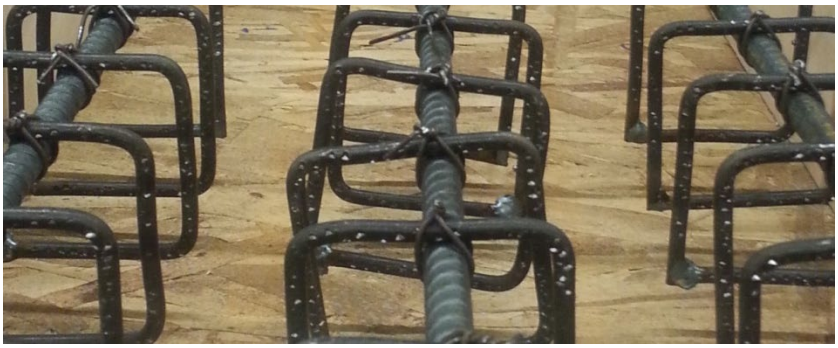

Figure 2.2 Shear stirrups with surface texture shown

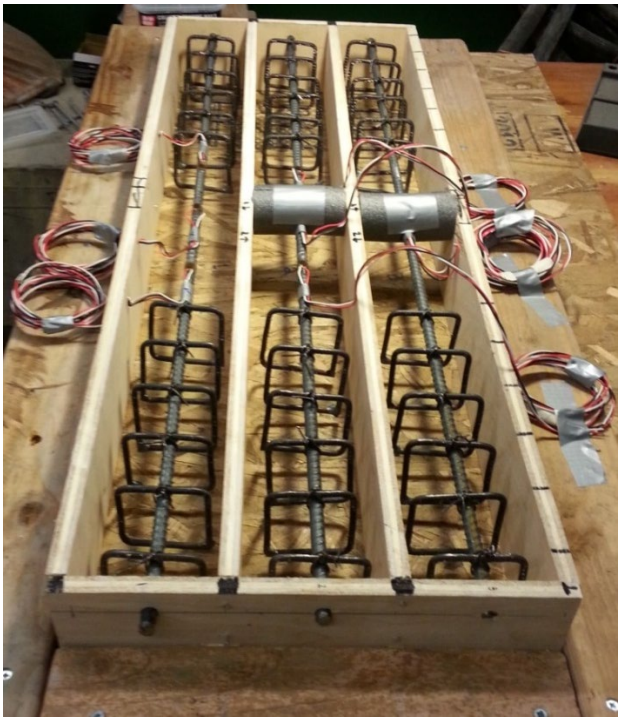

Figure 2.3 Small-scale beam forms with foam cylinders for access holes

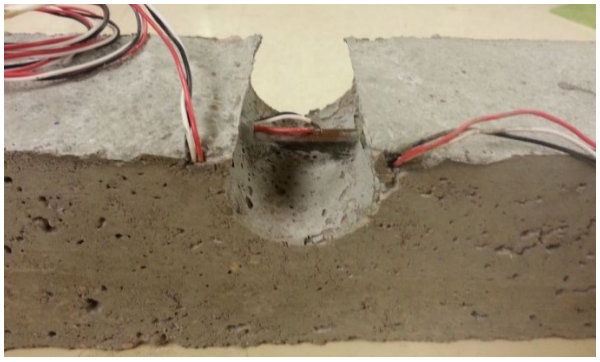

Figure 2.4 Small-scale beam with rebar access hole

2.1.2 Instrumentation

Instrumentation used for the small-scale beams consisted of 350 Ω foil backed strain gages attached to the single longitudinal bar. The ribs on the rebar were ground down and the surface smoothed using silicon carbide paper as per the installation instructions of the strain gage manufacturer as seen in Figure 2.5. Prior to concrete placement lead wires were soldered to the strain gages and a protective coating applied to eliminate damage to the strain gages during concrete placement.

A picture of the strain gage layout on each beam is shown in Figure 2.6. The stain gage layout was used so tensile stresses developed in the reinforcement could be determined in and outside of the removed concrete section to ensure stresses in the beams with and without access holes were acceptably close in value. Theoretically the stresses should be the same, up to yielding of the reinforcement, since the beam was loaded in four-point bending and the gages were all in the constant moment region.

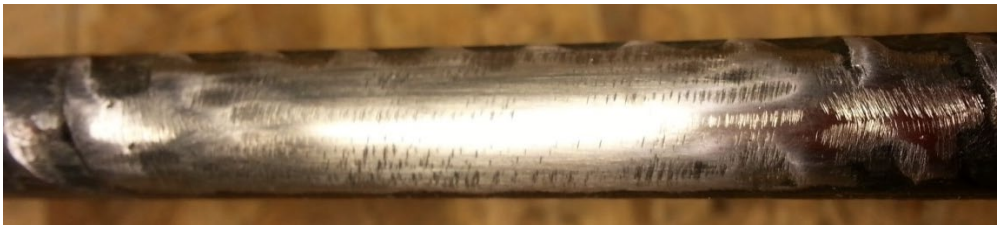

Figure 2.5 Deformed steel reinforcement with ribs ground down and sanded

Figure 2.6 Stain gage layout

2.1.3 Testing

The cured beams, shown in Figure 2.7, were tested monotonically to failure under four-point bending with the span between loading points being 305mm and the span between supports being 813mm. Applied force and displacement was measured internally by the United Testing Systems universal testing machine. The strain measurements were made by attaching the strain gage lead wires to a Campbell Scientific CR1000 data logger. In addition to ensuring the stresses in the rebar were similar, the strength and deflection of each beam was determined. Furthermore, the applied force and measured deflection of each beam was used to determine the stiffness variations between beams.

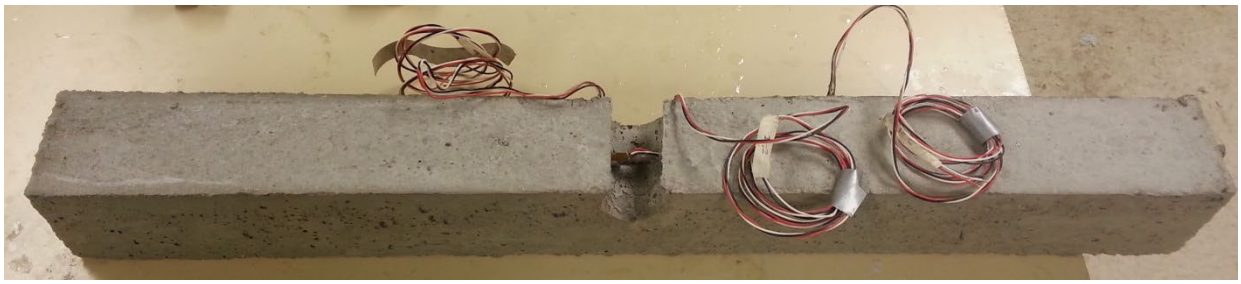

Figure 2.7 Cured small-scale beam with access hole and strain gage lead wires shown

2.1.4 Small-Scale Results

Test results showed all three beams had very similar load-deflection curves with negligible differences in stiffness in the elastic range and comparable strain levels in the rebar prior to yielding. While the data does show Beam 1 yielding at a lower load level than Beam 2, because the fatigue tests for the full-scale beams were to be run well below the level where rebar yielding would occur, this test showed good agreement with thinking the void in the concrete wouldn't affect the fatigue performance of the beams.

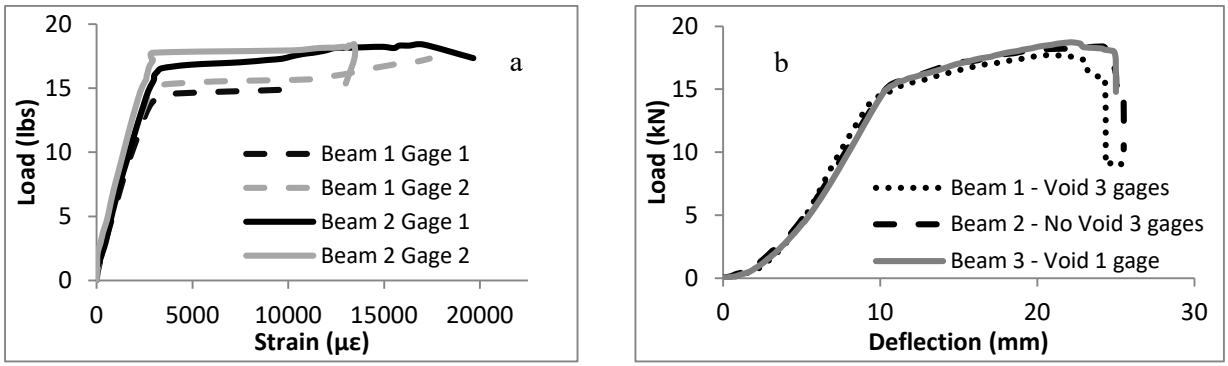

Figure 2.8 a) Small-scale beam load vs. deflection curve, b) small-scale beam load deflection curves

2.2 Full Scale Experimental Test Program

The large-scale experimental program consisted of seven beams to be fatigue tested, while a total of 10 beams were fabricated, three beams were for a similar project. The beams were divided into three groups in addition to a control beam; a non-CFRP strengthened group, a typical modulus CFRP sheet strengthened group, and a high modulus CFRP strip strengthened group. The following sections detail the design, fabrication, testing set up and instrumentation layout of the experimental test specimens.

2.2.1 Test Matrix

Ten 4,725-mm long, 250-mm wide, and 440-mm deep RC beams, were constructed for the experimental fatigue testing program. The fatigue performance of seven specimens—three with no CFRP retrofit and four with CFRP retrofit, all tested at ambient temperature—was discussed in Sobieck et al. (2014). The remaining three specimens, retrofitted with CFRP, were tested at elevated service temperature. The fatigue testing results of three recent specimens and four specimens reported in Sobieck et al. (2014) are presented in this article to assess the effects of high service temperature on fatigue life of CFRP-retrofitted RC beams. Table 2.1 summarizes the main characteristics of the seven specimens considered in the present study.

Table 2.1 Summary of experimental beam variations

*Specimen	Concrete Void	Rebar Strain Gauges	CFRP	**Avg. Temp.	Study
Beam 2	Yes	One on each No. 19 at mid-span and 150mm off center, 6 total	None	20ºC	Sobiek et al. (2014),
Beam 3	Yes	One on each No. 19 at mid-span and 150mm off center, 6 total	None	20ºC	Sobiek et al. (2014),
Beam 4	Yes	One on each No. 19 at mid-span and 150mm off center, two on CFRP, 8 total	Tyfo SCH-41 Sheet	20ºC	Sobiek et al. (2014),
Beam 5	Yes	One on each No. 19 at mid-span and 150mm off center, two on CFRP, 8 total	Tyfo SCH-41 Sheet	20ºC	Sobiek et al. (2014),
Beam 6	Yes	One on each No. 19 at mid-span and 150mm off center, two on CFRP, 8 total	Tyfo SCH-41 Sheet	40ºC	Current
Beam 7	Yes	One on each No. 19 at mid-span and 150mm off center, two on CFRP, 8 total	Tyfo SCH-41 Sheet	38ºC	Current
Beam 8	Yes	One on each No. 19 at mid-span and 150mm off center, two on CFRP, 8 total	Tyfo SCH-41 Sheet	31ºC	Current

Note: *Beams 2-5 in this study were labeled "Beam 2-5" in Sobiek et al. (2014).

**The average temperature values above 20ºC were selected to reflect a range of 30°C (86°F) to about 40°C (104°F), which is not uncommon in many states in the summer season.

All beams were fabricated with two A615M Gr. 420 No. 10 compression bars, three A615M Gr. 420 No. 19 tension bars, and a total of eighteen A615M Gr. 420 No. 10 shear stirrups as shown in Figure 2.1 and Figure 2.2. The stirrups were spaced at 170mm in the shear spans of each beam – Figure 2.2. Concrete was supplied by a local concrete batch plant with a 28-day compressive strength of 33 MPa. In beams 2-10, a small 90mm deep and 100mm wide cylindrical void was cast into the concrete, Figure 2.3, which allowed for a digital microscope to be placed in the void so images showing the cracked rebar could be captured. The images were later post-processed to determine the crack growth rate. It was anticipated that the void in the concrete would have negligible effect on the performance of the beam during the fatigue test because the applied cyclic loading would be higher than the theoretical concrete cracking moment essentially making the void a wide flexural crack. This was experimentally verified as outlined in Sobiek et al. (2014).

The purpose of the study was to evaluate crack growth as opposed to crack initiation, an approximately 2mm notch was cut into the two-exterior tensile rebar at mid-span of all beams. The notch size of 2mm was selected such that the resulting ΔK value is larger than ΔKth to ensure that crack growth would occur. The 2mm depth of the notch also represents a corrosion pit, using Eq. (5), which would have formed in a highly corrosive environment, at a much-localized point such as a flexural crack in the concrete, over 20 years. The notch was initially made using a cutting wheel and further sharpened using a utility knife blade to ensure faster crack growth initiation. The surface of the rebar was polished to remove the mill scale so a more accurate determination of the crack tip location could be made.

Beams 4-8 were externally strengthened with commercially available CFRPs. The tensile surface of beams was prepared for the application of CFRP by using a diamond cup grinding wheel to expose aggregate surfaces. All five beams were strengthened with the CFRP sheet. The fabric sheet was saturated with the epoxy and applied to the prepared beams via a hand lay-up process. The width and thickness of CFRP in all five specimens were 190 mm and 1mm, respectively. It is important to note that the CFRPs extended beyond the supports so that end-peel is prevented. This is intended to simulate mechanical clamping of the CFRP at the end of the beam—a typical field practice. This approach was deemed acceptable since the focus of the study was on the effect of loss of stiffness in the adhesive, as oppose to CFRP end peeling, on fatigue life.

2.2.2 Specimen Design

All test beams were designed with the same dimensions and internal steel reinforcement using ACI-318: Building Code Requirements for Structural Concrete. Length of the specimens was controlled by the size of the testing frame. From there the depth was chosen to ensure the beam didn't fall under deep beam conditions, and a width picked to produce a rectangular cross-section which is typical for RC beams and agreed well with previous research. Adequate concrete cover was also taken into account when dimensioning the beam cross-section. The steel reinforcement amount was chosen to produce an under-reinforced beam that would fail in flexure. While compression reinforcement wasn't needed for strengthening purposes, fabrication of the reinforcing cages was easier with them. Additionally, since the beams were to be fabricated in an inverted position so the FRP could be applied to the tensile soffit of the beam, the compression bars were needed to provide a place for the rebar chairs to elevate the cage off the bottom surface of the forms. The shear stirrups were needed to resist diagonal-shear cracking, which would have been the controlling failure mode at the given loadings.

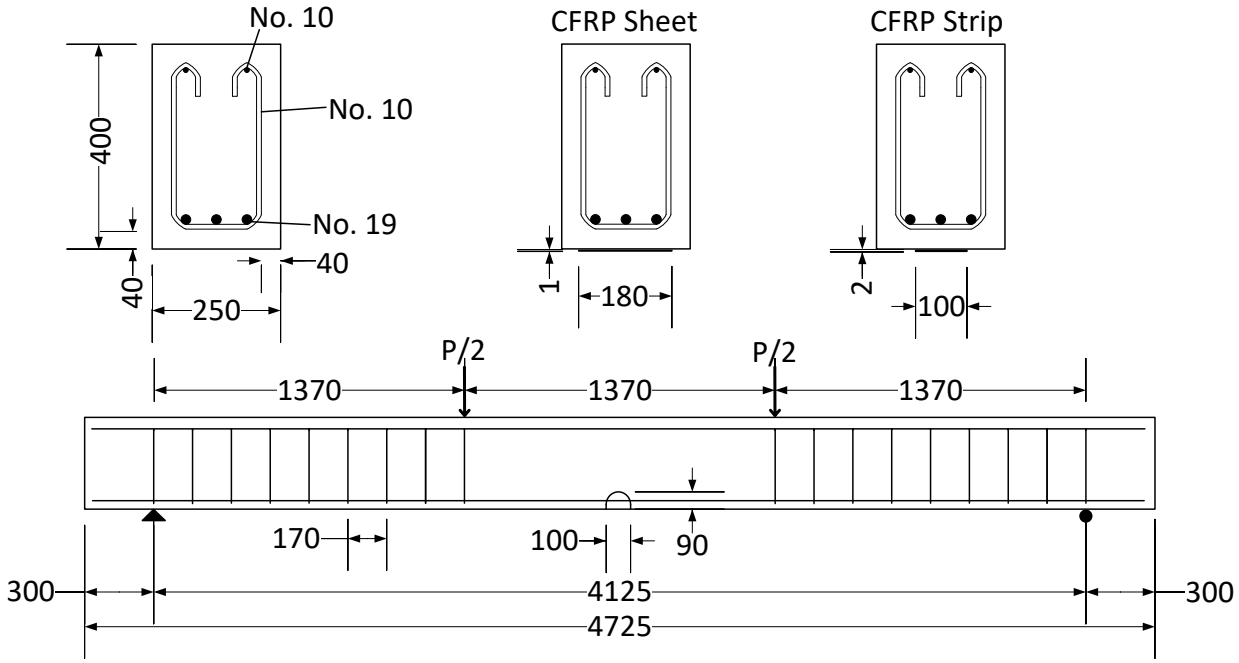

Figure 2.9 Experimental test specimen details

The notch cut into the tensile reinforcement was sized using Equation 1.10 to represent a corrosion pit which would have formed in a highly corrosive environment, at a very localized point, such as a flexural crack in the concrete, over 20 years. This gave a notch depth of approximately 2mm. This value was checked with Equation 1.5 to ensure this notch would be able to produce a stress intensity factor range higher than the threshold value, allowing fatigue crack growth.

To investigate the difference in designing a FRP repair for strength versus fatigue, the beams in groups 3 and 4 were both repaired to the same nominal moment carrying capacity using Equation 10-13 from ACI 440.2 with two different CFRP types. The beams in group 3 (4 and 5) were strengthened using a CFRP sheet while the beams in group 4 (6 and 7) were strengthened using a CFRP pressured strip. Since it was easier to vary the width of the CFRP sheet, the moment capacity for a beam strengthened with the CFRP strip was determined. Then the width of the CFRP sheet— able to provide the same strength—was solved. The factored nominal moment capacity for beams 1, 2, and 3 was 115.9 kN-m, for beams 4 and 5 the capacity was 150.26 kN-m and for beams 6 and 7, 150.19 kN-m was calculated. Whereas the moment capacity of the unstrengthened beams was governed by yielding of the steel rebar, the moment capacity of both strengthened beams was governed by the debonding of the CFRP. In the strengthened beams, the yield strain of the steel rebar is reached first followed by the predicted debonding strain of the CFRP, while the concrete strain remains below the ultimate strain until after the CFRP debonds.

The applied load range between 40 kN and 100 kN gave a predicted stress range in the tensile steel reinforcement of 150 MPa for the unstrengthened beams, 130 MPa for the Tyfo SCH-41 strengthened beams, and 120 MPa for the Tyfo UC strengthened beams. These values were obtained using Equation 10-14 from ACI 440.2 and general section analysis calculations, which is shown below in Equation 2.1.

$$\sigma_{s,s} = \frac{\left[M_s+\varepsilon_{bi}A_fE_f\left(d_f-\frac{kd}{3}\right)\right](d-kd)E_s}{A_sE_s\left(d-\frac{kd}{3}\right)(d-kd)+A_fE_f\left(d_f-\frac{kd}{3}\right)(d_f-kd)} \tag{2.1}$$

Table 2.2 Variable definitions and units

Variable	Unit	Definition
$\sigma_{s,s}$	MPa	Steel stress at service moments
ε_{bi}	m/m	Strain level in concrete substrate at time of FRP installation
E_f	MPa	Tensile modulus of elasticity of FRP
k	---	Ratio of neutral axis depth to reinforcement depth measured from extreme compression fiber
E_s	MPa	Modulus of elasticity of steel
M_s	MN.m	Service moment at the section of interest
A_f	M^2	Area of FRP external reinforcement
d_f	m	Effective depth of FRP flexural reinforcement
d	m	Distance from extreme compression fiber to centroid of tension reinforcement

2.2.3 Specimen Fabrication

The test beam specimens were fabricated in the structural engineering lab at the Colorado State University Engineering Research Center directly adjacent to the testing frame. Form-work was constructed out of 19mm thickness plywood and lumber 2x4s, shown in Figure 2.10. The formwork was assembled in such a way so the walls could be removed after the concrete had cured so application of the CFRP could occur and the beams could be picked up and individually loaded into the testing frame.

Figure 2.10 Braced plywood and lumber form-work

In addition to the walls and bottom of the form-work, foam tubes were used to form a 90mm deep and 100mm wide cylindrical void into the concrete to expose the No. 19 tensile rebar at mid-span of beams 2-6, which allowed access for a digital microscope to track the crack growth rate, as shown in Figure 2.11. Again, the beams were fabricated in an inverted position to allow access to the tensile soffit of the beam for FRP application; therefore, the voids were cast in the relative top of the beams. The void in the concrete offset relative to the notch at mid-span to allow nominal strain in the rebar in the void to be measured via a strain gage. The void was offset to keep the strain gage away from any stress concentration cause by the notch while also keeping the void to a minimal size.

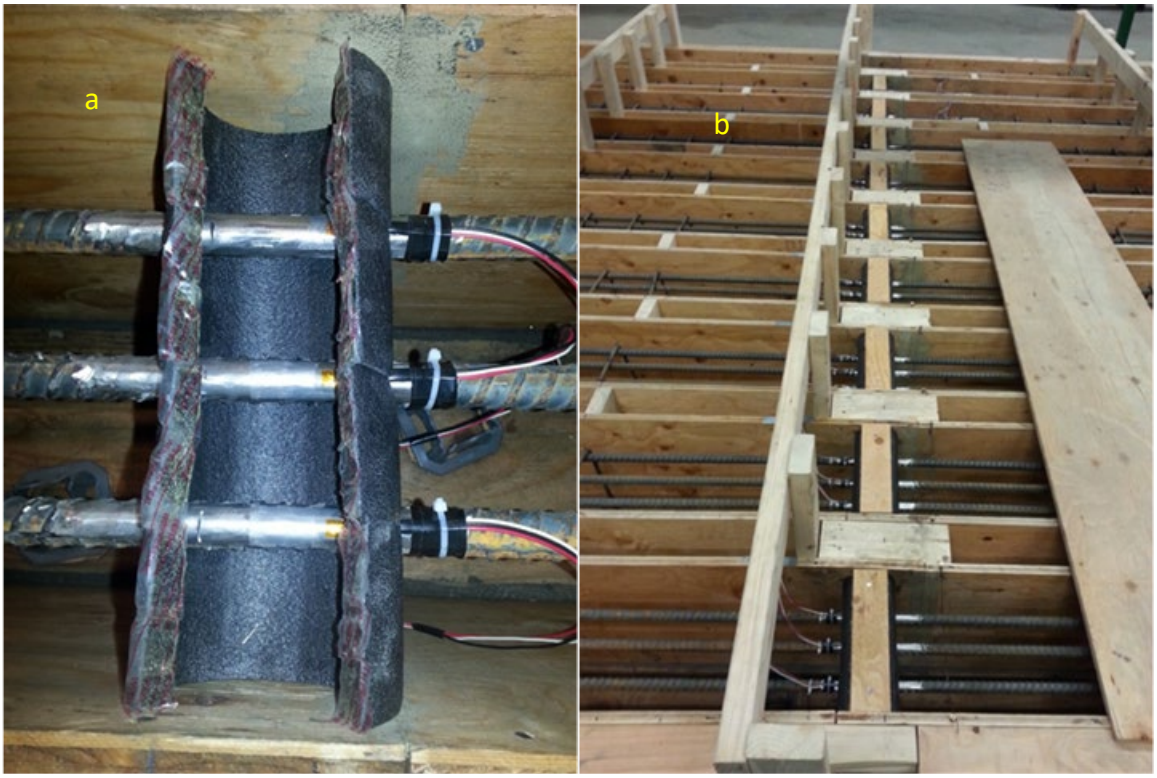

Figure 2.11 a) Foam tube used to form void at mid-span, shown with notches cut in outer-most rebar, b) Foam void forms with lumbar caps in beams 2-10

The steel rebar cages were tied up and lowered into the forms with the No. 19 rebar on the relative top. The cages rested on plastic rebar chairs to achieve the concrete cover needed shown in Figure 2.12b. Once the cages were in the forms, the ribs on the No. 19 rebar were removed for a length of 150mm at midspan and in beams 2 and 3 at an additional location 230mm away. The purpose for these additional smoothed portions is explained later in the Instrumentation section. The ribs were removed and the surface polished not only to give the strain gages a smooth surface to attach to, but also to make propagation of a fatigue crack from the cut notch more easily visible. The notches were cut into the outer most No. 19 rebar after polishing using a Dremel tool with a silicon carbide cutoff wheel with marking of 2mm to ensure all notches were cut to approximately the same depth. A rounded notch tip was left by the cutting wheel; therefore, a utility knife blade was used to sharpen the notch tip to preserve the higher stress intensity.

Figure 2.12 a) Rebar cages, b) 40mm plastic rebar chairs, c) position of rebar cage in form, d) depth of tensile reinforcement once supported on 40mm rebar chairs

Concrete was supplied by a local concrete batch plant and placement of the concrete for all beams was performance in the same day. A concrete vibrator, shown in Figure 2.13, was used to ensure minimal voiding between the rebar cages and form walls, and around and in the rebar chairs. The concrete was allowed to cure 28 days before the form-work was removed and testing began.

Figure 2.13 Concrete placement

Application of the CFRP didn't occur until the concrete reached the 28-days compressive strength. Four beams were externally strengthened with commercially available CFRPs produced by Fyfe Co. Prior to application of any CFRP, a diamond cup grinding wheel was used to remove the concrete laitance layer (about 5mm) from the soffit of each beam to expose the aggregate and promote a stronger bond between the concrete and CFRP, Figure 2.14. Beams 4 and 5 were strengthened with a 190mm wideTyfo SCH-41 uni-directional carbon fabric sheet and Tyfo S Epoxy. The fabric sheet was saturated with the epoxy and applied to the prepared beams via a hand lay-up process shown in Figure 2.15. Beams 6 and 7 were strengthened with a single Tyfo UC strip, which is a high modulus, high tensile strength, pultrusion fabricated carbon-epoxy laminate. The Tyfo UC strips were adhered to the concrete substrate with Tyfo TC Epoxy, shown in Figure 2.16.

Figure 2.14 Concrete surface, top; removed laitance layer exposing aggregate, bottom; concrete surface left by finishing of wet concrete

Figure 2.15 Hand-layup process of Tyfo SCH-41 CFRP sheets and beams 4 and 5

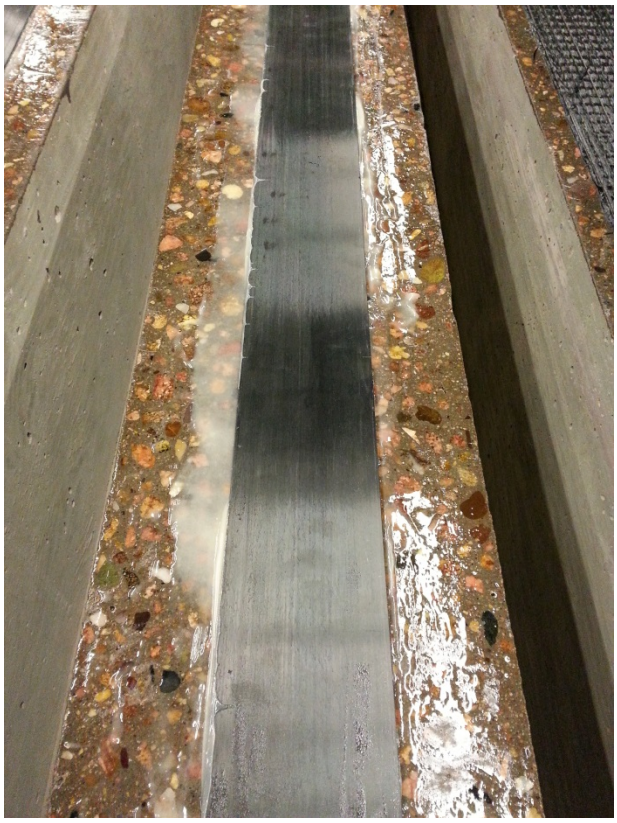

Figure 2.16 Tyfo UC CFRP strip

2.2.4 Material Properties

The concrete was allowed to cure for 28 days. Cylinder compression tests were performed at 7, 14, and 28 days. In addition, a test was performed at the half-way point through testing. At each testing day, three cylinders were tested to determine an average value. The results were then used to produce a compressive strength curve so the concrete compressive strength for each beam could be determined the day the specimen was tested. In Table 2.3, the values for the compressive strength are the average of each beam in the group. Properties for the CFRP and steel reinforcement are also given.

Table 2.3 Experimental beam material properties

Material Properties	Unstrengthened Beams 1,2, and 3	Tyfo® SCH-41 Sheet Beams 4 and 5	Tyfo® UC Strip Beams 6 and 7
Concrete compressive strength (MPa)	32.82	33.23	33.35
Rebar Tensile Yield Strength No. 10/No.19 (MPa)*	491/481	491/481	491/481
CFRP Tensile Strength (MPa)*	N/A	986	2790
CFRP Tensile Modulus (GPa)*	N/A	95.8	155
CFRP Elongation at Break (%)*	N/A	1.0	1.8
CFRP Width (mm)	N/A	190	100
CFRP Thickness (mm)	N/A	1	2
Epoxy Tensile Strength (MPa)*	N/A	72.4	22.7
Epoxy Tensile Modulus (GPa)*	N/A	3.18	1.2

* Properties provided by manufacturer

2.2.5 Test Setup and Instrumentation

All beams were loaded at clear-span third points, 1,370mm from each support, through a spreader-bar by a single 160 kN capacity MTS servo-hydraulic actuator, Figure 2.17a. The actuator was controlled using an MTS Flex test GT whose control software was configured to collect the applied load, actuator extension, and cycle count data at each load cycle peak and valley. The high service temperature was applied to beams 6-8 using three pairs of radiative heating panels located on both sides of the beams as shown in Figure 2.17a. A power control panel, Figure 2.17c, was programmed to provide a constant power to the heating panels to generate constant temperature during the fatigue tests.

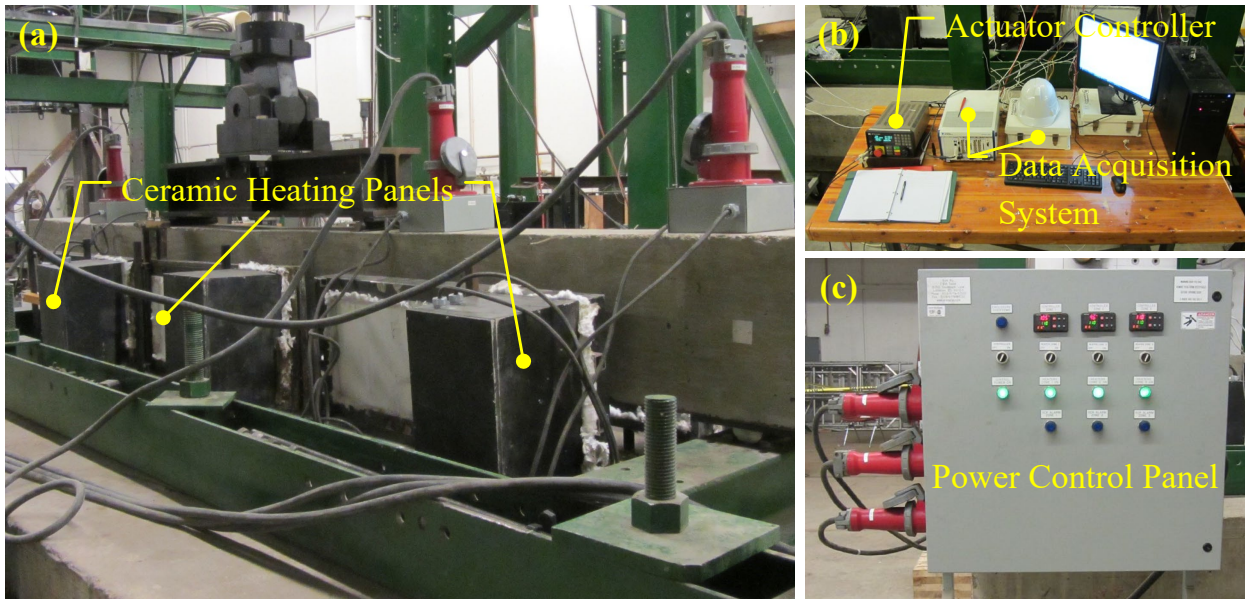

Figure 2.17 (a) RC beam with side heating panels and loading actuator, (b) actuator controller and data acquisition system, and (c) power control panel

Linear pots mounted to the beam at mid-span and at each loading point provided direct measurement of beam displacements. Foil backed 350Ω strain gages were attached to each No. 19 rebar 65mm from the notch cut at mid-span. Beams 2 and 3 had additional strain gages attached to the No. 19 rebar 400mm off from mid-span for strain comparison purposes in the constant moment region. In addition, a single strain gage was attached to the concrete surface on top of each beam at mid-span and two strain gages were applied to the CFRP in the constant moment region, one directly over the void and the other 230mm away. All instrumentation was wired to Campbell Scientific CR1000 data loggers for data collection.

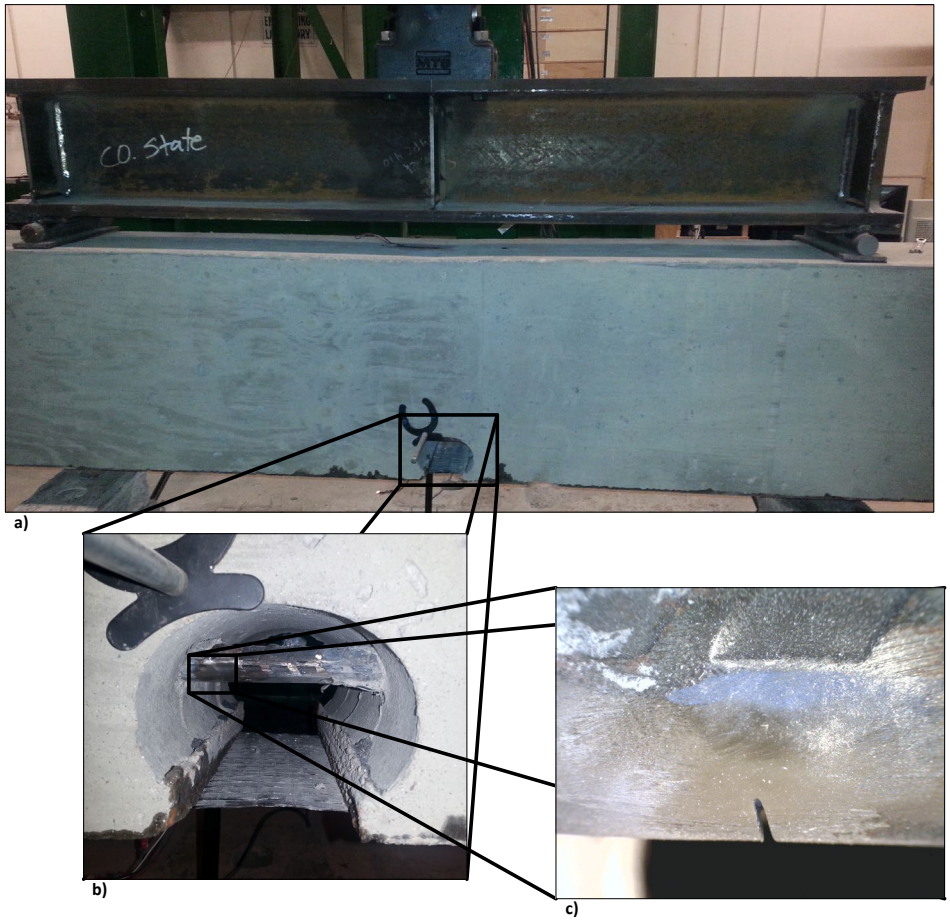

Figure 2.18 a) Constant moment region of beam showing loading apparatus at top and void in concrete exposing tensile rebar, b) void showing CFRP sheet (bottom centre) and digital microscope mount (top left), and c) notch and polished surface of rebar at mid-span

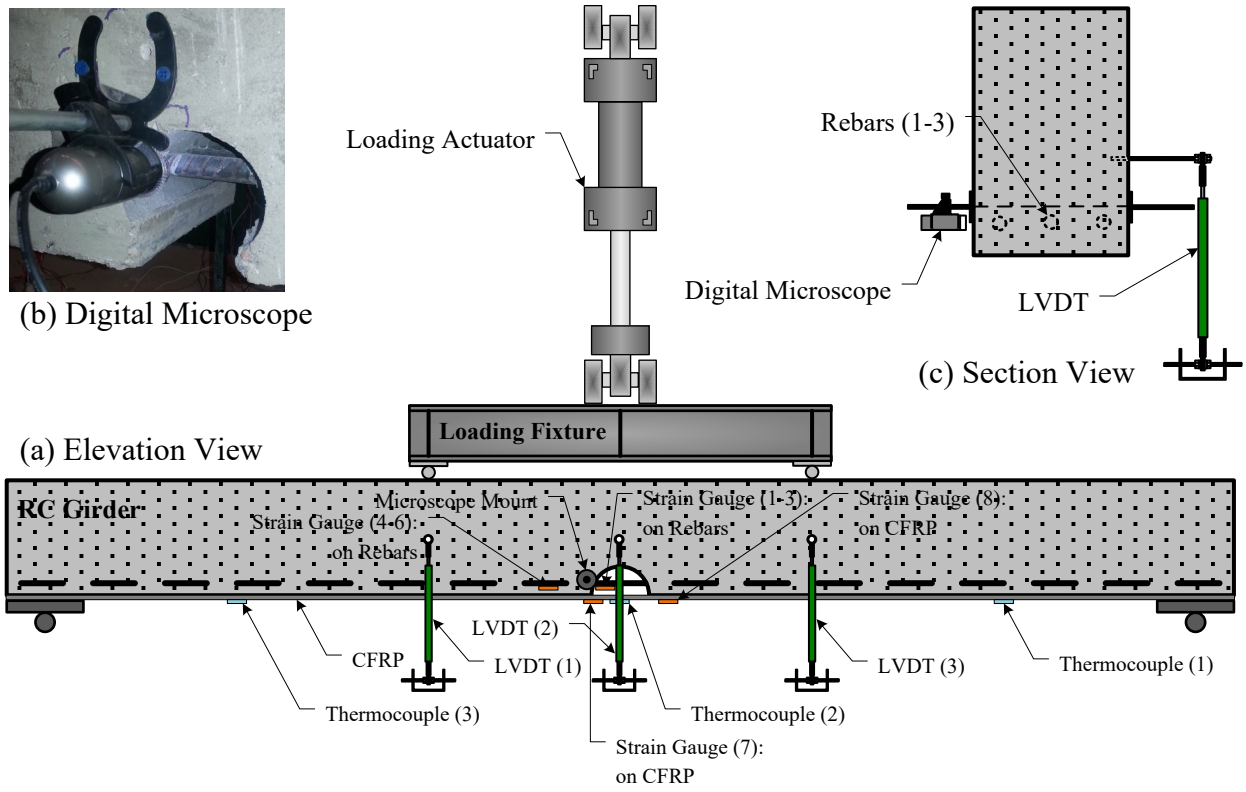

Figure 2.19 a) Elevation view of the experimental set up and the instrumentation plan, b) digital microscope, and c) section view of the set up

Crack length measurements were made using a digital microscope. The microscope was attached to the side of the beam allowing for a profile image at approximately 20 times magnification to be taken of the rebar closest to the sides of the beam. Based on the magnification, dimensions of the crack could be measured from the image using a companion software.

2.2.6 Testing Procedure

All beams were subjected to cyclic loading in the form of a sine wave under force control at a frequency of 2.5 Hz. Beams 2-8 were loaded at an increased range of 40 kN – 100 kN. Two slower cycles, at a frequency of 0.05 Hz, were applied to the beam at the first two cycles and every 50,000 cycles afterwards. These slow cycles allowed for a more refined data set to be collected, approximately 56 scans per slow cycle, and allowed for the digital microscope to be switched to both sides of the beam to view the most exterior No. 19 bars. In addition, the condition of CFRP was carefully assessed during the slow cycles with respect to any rupture or debonding.

In addition to cyclic loading, a constant service temperature was applied to beams 6-8. Beams 2-5 were tested only at ambient temperature (Sobieck et al. 2014). On average, the high service temperature ranged between approximately 30°C and 40°C as outlined in Table 1. This range of temperature was selected to represent high temperatures that CFRP repaired beam might realistically be subjected to in service. It is noted that beams 6-8 were pre-heated to ensure a constant service temperature prior applying the cyclic loading. The applied thermal load was kept constant during the entire fatigue tests to simulate worst case

scenario where the increased temperature would have detrimental effect on the adhesive, thereby reducing the effectiveness of the CFRP.

2.3 Validity of Thermal Loading in the Presence of a Void

In the experimental study, thermal panels were used, as will be discussed later in more details, to apply the desired temperature in the steel rebar in the presence of the void. To evaluate validity of this approach in comparison to reality where there is no void, numerical simulations were conducted. Specifically, numerical transient heat transfer analysis was conducted using ABAQUS 6.14 (ref.) to 1) evaluate heat penetration into the steel rebar through the concrete, 2) the expected time required to reach the applied temperature, and 3) the temperature variation between the steel and the concrete. The numerical model comprised of 4-node heat transfer quadrilateral shell elements (DS4). Thermal conductivity, specific heat, and density were considered as 1.75 W/m.K, 0.92 KJ/kg.K, and 2300 kg/m3, respectively, for the concrete and 54 W/m.K, 0.49 KJ/kg.K, and 7850 kg/m3, respectively, for the steel . Three edges of the concrete beam, as highlighted in Figure 2-20, are exposed to 40, 38, and 31° C to represent Beam 6, 7, and 8, respectively. Figure 2.20 shows the heat propagation contour throughout the concrete at one-hour intervals. Additionally, Figure 2.21 shows the temperature versus time at the location of the highlighted rebar. It was observed that the temperature in the rebar reaches the desired temperature, which was applied to the concrete external surfaces in approximately three hours, although the temperature of the exterior rebar is at 90 percent of the ultimate value in an hour. In other words, in the absence of a void, representing reality, the steel rebar is expected to reach the concrete surface temperature in the range of one to three hours. Therefore, applying such temperature in the presence of a void is a reasonable representation of reality.

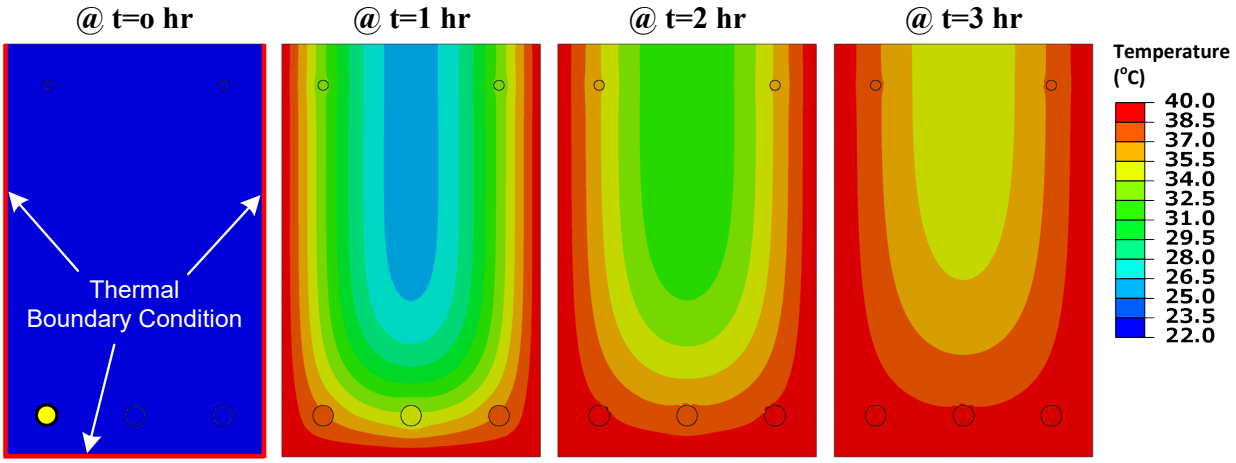

Figure 2.20 Temperature contour in the concrete at different time intervals

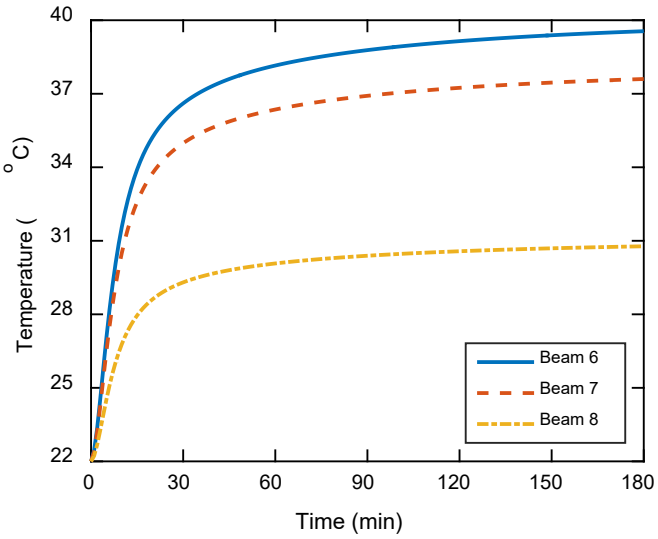

Figure 2.21 Temperature variation at the exterior rebar

3. RESULTS AND ANALYSIS

3.1 Effect of Void in Concrete

The significance of the void in the concrete with respect to the structural performance of the beam was extensively investigated by Sobieck et al. (2014). It was concluded that the addition of the void decreases the average beam stiffness by only about 4.5 percent during the cyclic test.

The effect of the void on the measured rebar strains is investigated for Beams 2 and 3. There are two strain gauges installed on each tensile rebar, one located in the void (strain gauges 1 to 3) and one embedded in the concrete with 150mm (6 in) distance (strain gauges 4 to 6). Figure 3.1 shows comparison between the strain ranges in the three tensile rebar both inside the void and embedded in the concrete for Beams 2 and 3. The lower measured strain values in Beams 2 are attributed to the higher stiffness of Beams 2 at the 50,000-cycle mark. These strain ranges are only assessed at this point because shortly after the 50,000-cycle mark the rebar strain gauges embedded in concrete started to fail due to flexural cracking of the concrete causing the lead-wires to pull away from the gauges.

Figure 3.1 indicates a linear correlation between strain range in the rebar measured by strain gauges located in the void and in the concrete. It is observed that the strain range in the rebar located in the void is higher than the strain measured by the gauge embedded in the concrete despite both locations being in the constant moment region along the length of beams. While these results indicate that the void did have an impact on the structural performance of the beams, the degree of this impact is minor, especially for the purpose of the study. The study focuses on the comparison of the CFRP repairs on the beams, all of which had voids in the concrete. Additionally, strain measurements are made within the void near the location of the notch, where rebar crack growth occurred, allowing the nominal stress at the location of the crack to be determined.

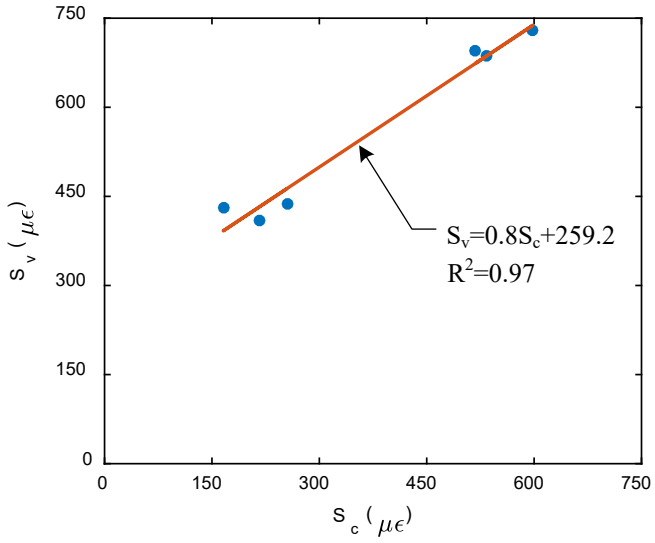

Figure 3.1 Strain ranges in the three tensile rebar inside the void (Sv) and embedded in the concrete (Sc) for beams 2 and 3

3.2 Observed Fatigue Performance

All beams failed due to fatigue induced fracture of one or more of the notched tensile No. 19 rebar. A depiction of the fatigue crack growth process is shown in Figure 3.2 for rebar 1 in Beam 7. Beams 2, 3, and 6 experienced fatigue crack growth in both notched rebar, while in the remaining beams fatigue crack propagation occurred in only one of the notched bars despite continuing the testing for a minimum of 50,000 cycles after the fracture of the first rebar. In Beams 2, 3, and 6, the presence of a visible crack in the other exterior notched rebar occurred prior to the fatigue induced fracture of the first rebar. Additionally, the number of cycles between fracture in both rebar in beams 2, 3, and 6 was less than 50,000 cycles. Immediately following fracture of the second notched rebar, the third, middle rebar yielded and large flexural cracks, extending from the concrete void, ensued as shown in Figure 3.3a for Beam 6. Figure 3.3b shows full fracture in rebar 1 of Beam 6 while Figure 3.3c and Figure 3.3d show rupture and debonding, respectively, in the CFRP of the Beam 6 at the end of the fatigue test. It is noted that the major CFRP rupture and debonding occurred at the end of fatigue test when Beam 6 experienced large deflections, although localized rupture in the CFRP or debonding with variable length was observed during the cyclic loading. Figure 3.4 shows the fractographic profile for the rebar fractured in Beams 6-8 that were tested at high service temperatures. A similar trend was observed for fatigue and fracture surfaces, with thumbnails indicating the sequence of fatigue crack growth.

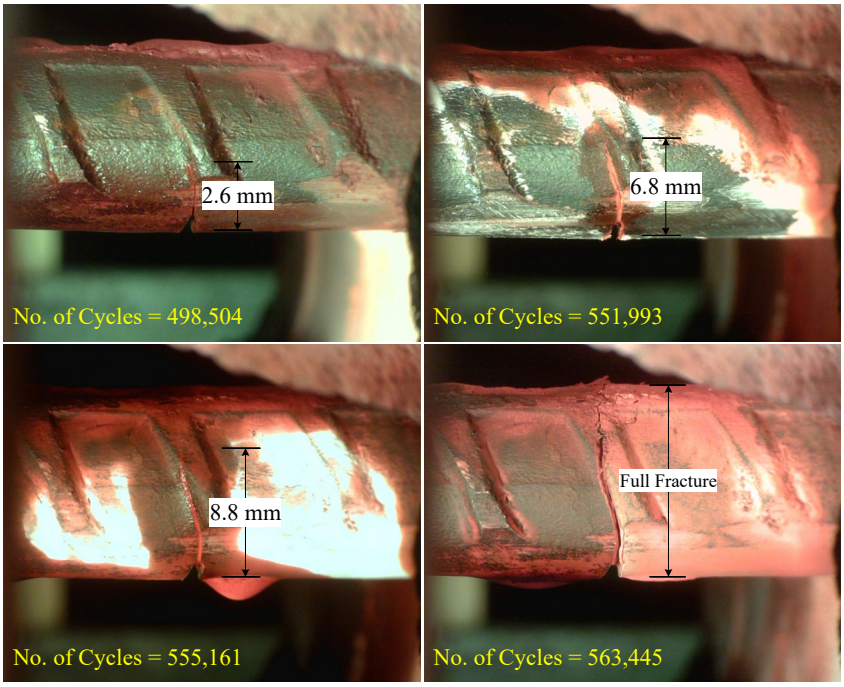

Figure 3.2 Depiction of the fatigue crack growth process for beam 7

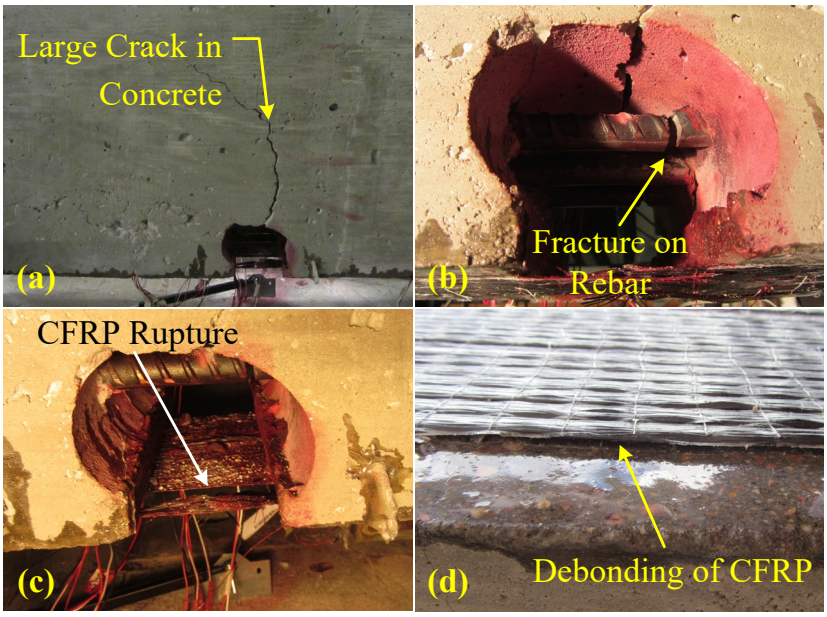

Figure 3.3 Depiction of the beam 6 at the end of the fatigue test: (a) large crack in the body of concrete extending from the void, (b) full fracture in rebar 1, (c) rupture of the CFRP at the location of the void, and (d) debonding of the CFRP

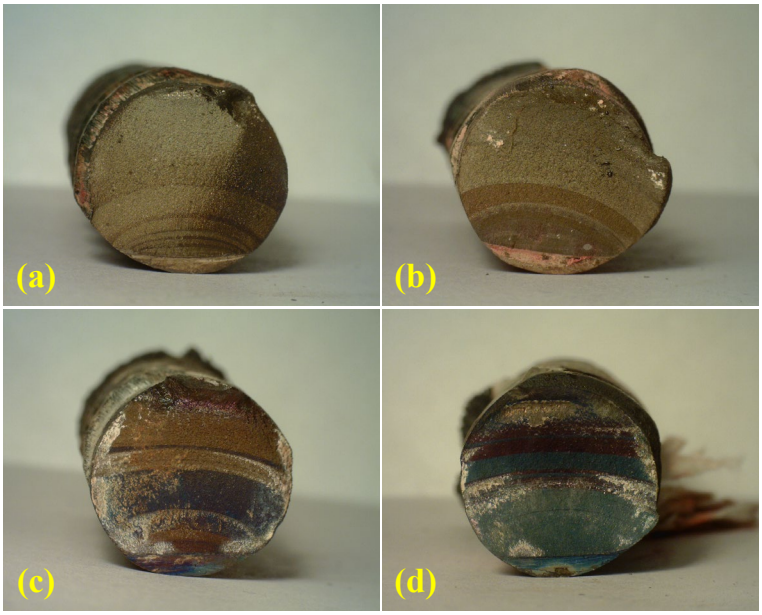

Figure 3.4 Fractographic profile for (a) rebar 3 beam 6, (b) rebar 1 beam 6, (c), rebar 1 beam 7, and (d) rebar 1 beam 8

The addition of the CFRP repair was observed to reduce the strain in the tensile reinforcement. The average rebar strain range during the entire fatigue test in Beams 2 and 3 (no FRP) was 530 and 584 με, respectively, while it was 437 and 480 με for Beams 4 and 5, respectively. An average reduction of 17.5 percent is observed in Beams 4 and 5 strengthened with the CFRP sheet and tested at ambient temperature. For Beams 6 and 8 strengthened with the CFRP sheet and tested at high service temperatures, the average strain range during the entire test is 545 and 507 με, respectively. The strain data collected for Beam 7 was not consistent; therefore, it was not included in the interpretation of the strain data. It is noted that the average strain range during the entire test for Beams 6 and 8 is between Beams 2 and 3 (no CFRP retrofitted) and

Beams 4 and 5 (CFRP retrofitted). It is attributed to the fact that although CFRP loses a fraction of its strength at high service temperatures; however, high service temperature creates compressive strain in the rebar, which results in reduction in the tensile strain in the rebar. It is noted that the difference in the strain range of the rebar between identical specimens, even though they were designed for the same flexural capacity, might be attributed to a slight difference in the application of the CFRP repair.

Just prior to any cracking in the rebar, a noticeable drop in the measured strain would occur. This drop was linear at first, but after the crack length exceeded 1mm the drop became exponential with continued cycling as shown in Figure 3.5. Additionally, as the strain in the fatiguing bar would drop the strain in the other two bars would increase, signifying a redistribution of stresses.

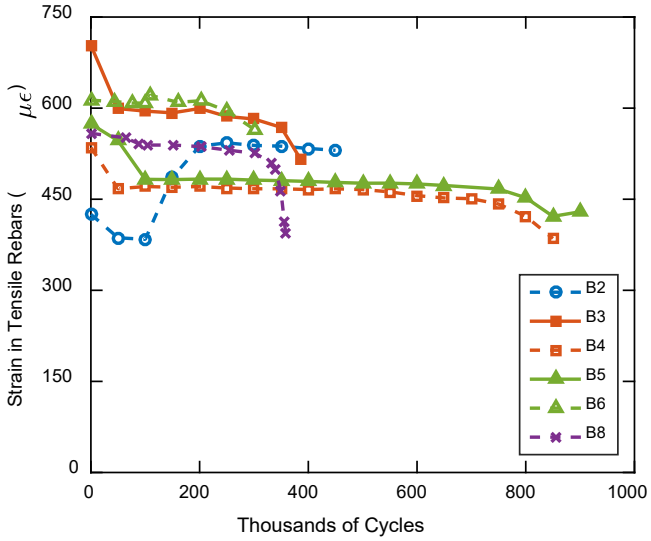

Figure 3.5 Strain range in the rebar during the cyclic fatigue testing

Finally, despite Kim and Heffernan (2008) reporting many studies experiencing issues with debonding of the CFRP along the length of beams especially with thicker and high modulus CFRPs, no debonding of any type was observed in the beams tested at the room temperature – Beams 4 and 5 – per Sobieck et al. (2014). At high service temperatures, CFRP debonding was observed in all beams 6 to 8. The debonding was localized and occurred at different locations along the length of the beams regardless of the applied moment at the location. The length of debonding was also variable such that a maximum of 305mm (1 ft) was observed in the Beam 7.

Figure 3.6a shows correlation between the strain ranges in the tensile rebar inside the void, Sv, and CFRPs, SCFRP, for Beams 4 and 5 tested at the room temperature while Figure 3.6b shows the same plot for Beams 6 to 8 tested at high service temperatures. As shown in the plots, small scatter is observed for beams tested at the ambient temperature, Figure 3.6a, while large scatter is noted for beams tested at high service temperatures, Figure 3.6b. Strains measured in the CFRPs of Beams 4 and 5 are four times larger than those measured in the CFRPs of Beams 6 to 8. This is attributed to the fact that debonding of the CFRPs in Beams 6 to 8 prevented the full development of axial demand in the CFRPs.

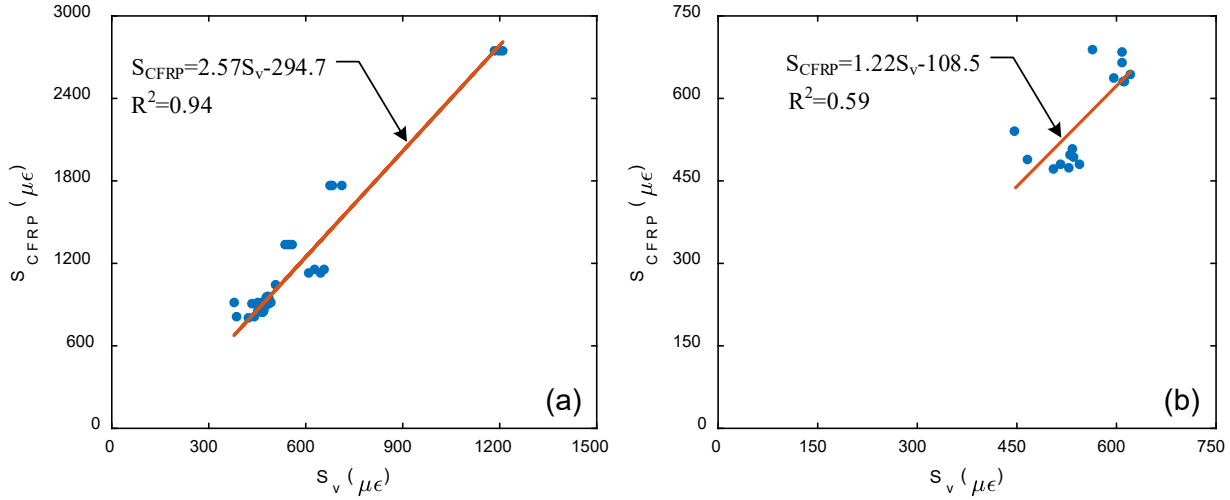

Figure 3.6 Correlation between strain in the tensile rebar and CFRPs at (a) room temperature and (b) high service temperature

3.3 Crack Propagation in Rebar

Figure 3.6 shows the crack length versus number of cycles for each beam over the entire test from the point where the crack first becomes visible, respectively. A general trend of increased fatigue life and slowed crack growth rate with the addition of CFRP can be seen per Figure 3.6. The fatigue life and crack growth rate for the SCH-41 sheet strengthened beam (4 and 5) are consistent as shown in Figure 3.7. Beam 6 shows improved performance over the SCH-41 system with a longer fatigue life and slowed crack growth rate, per Figure 3.7. Beam 7 and Beam 8 exhibit the best performance in terms of prolonged fatigue life, as seen in Figure 3.7. In general, the results show the benefit of adding CFRP for slowing down crack growth. Furthermore, the applied service temperature, in the tested range, appears to provide beneficial effect for increasing the fatigue life. This is because the increase in rebar temperature causes the rebar to want to axially strain and extend, which is naturally prevented by the surrounding concrete, which in turns imposes compressive forces on the rebar, promoting crack closure.

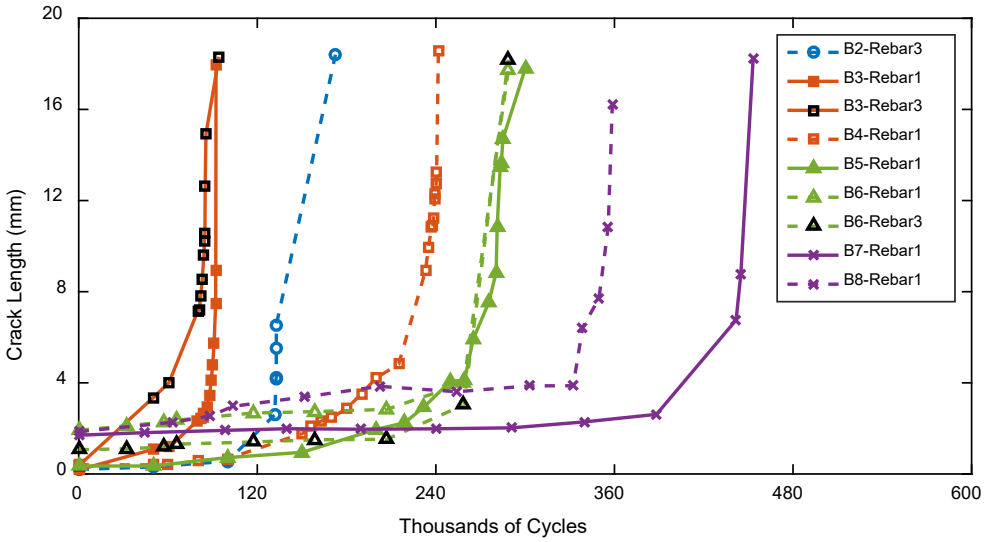

Figure 3.7 Crack length versus number of cycles when the crack is visible

3.4 Fatigue Parameter Analysis

Determination of the Paris Law parameter, constants C and m in Eq. (4), is useful for developing analytical solutions that can be used to predict the crack growth rate. The constants were determined from a log-log plot of the crack growth rate, da/dN, versus the stress intensity factor range, ΔK, for Beams 2 to 5 shown in Figure 3.8 and Beams 6 to 8 shown in Figure 3.9. The values for C and m are the y-intercept and slope of the power trend line shown on the plots, respectively. For Beams 2 to 5, the value for C is found to be 9.77×10-11, while the value for m is 2.36. For beams 6 to 8 tested at high service temperatures, the value for C is determined as 2.51×10-11, while the value for m is 2.99.

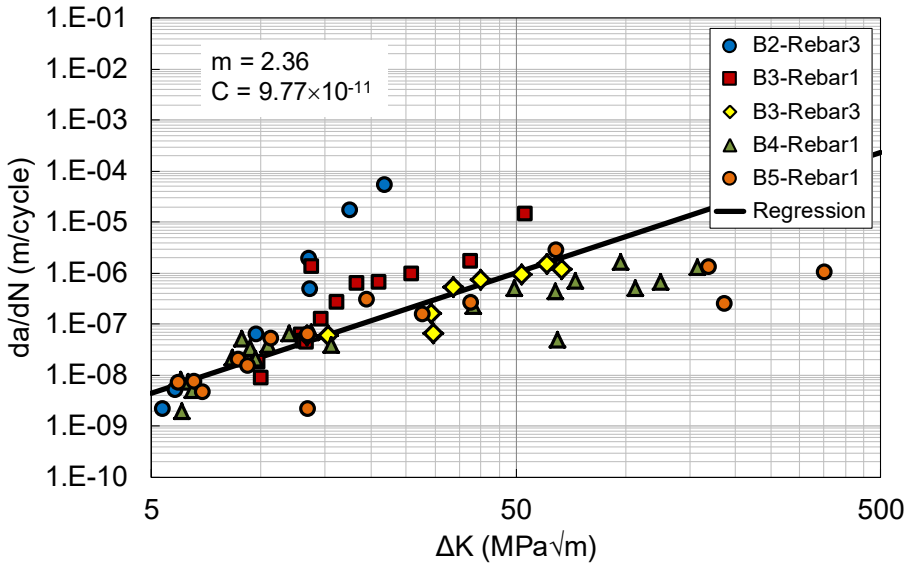

Figure 3.8 Crack propagation rate versus stress intensity factor range for beams tested at the room temperature

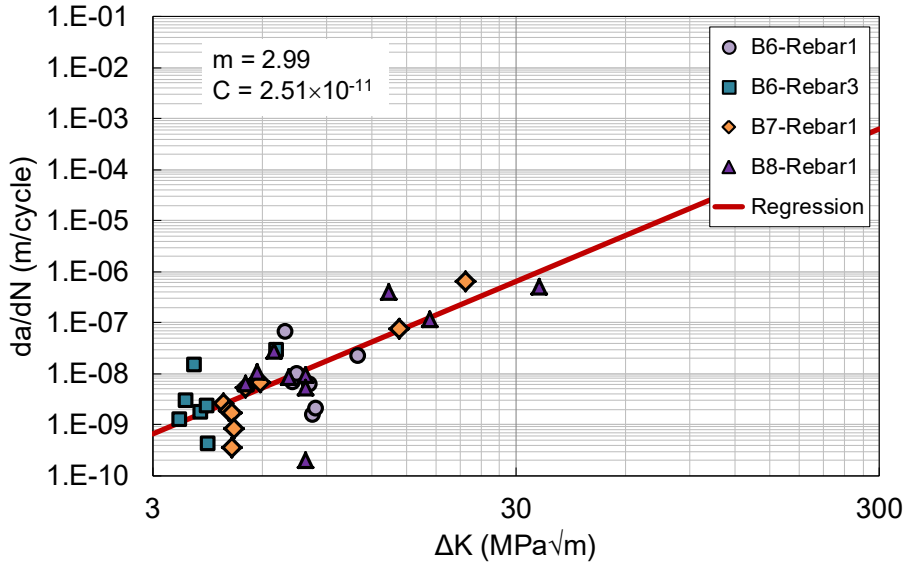

Figure 3.9 Crack propagation rate versus stress intensity factor range for beams tested at high service temperatures

4. CONCLUSION AND FUTURE WORKS

In this study, a unique experimental test was devised to directly measure fatigue crack propagation rates in the tensile steel reinforcement of full-scale RC beams with and without CFRP repairs. The results of the tests were then used to determine the material constants in the Pairs Law equation. Additional significant findings and characteristics of the study include:

- The strain range in the rebar located in the void was slightly higher than the strain measured by the gauge embedded in the concrete despite both locations being in the constant moment region along the length of beams, which indicates that the void did not have a significant impact on the structural performance of the beams for the purpose of the study.
- The addition of the CFRP repair was observed to reduce the strain in the tensile reinforcement.
- Although the CFRP did show localized areas of rupture or debonding at high service temperatures, the fatigue life of the specimens tested at high service temperatures was enhanced as the high service temperatures created compressive strain in the rebar, which resulted in reduction in the tensile strain in the rebar.
- No debonding of any type was observed in the beams tested at the room temperature – Beams 4 and 5. At high service temperatures, only local CFRP debonding was observed in all beams 6 to 8 with a maximum of 305mm (1 ft) that was observed in the Beam 7.
- A general trend of increased fatigue life and slowed crack growth rate with the addition of CFRP can be seen. Both the fatigue life and crack growth rate for the SCH-41 sheet strengthened beam (4 and 5) are consistent. Beam 6 shows improved performance over the SCH-41 system with a longer fatigue life and slowed crack growth rate. Beam 7 and Beam 8 exhibit the best performance in terms of prolonged fatigue life.

In general, results show the benefit of adding CFRP for slowing down crack growth. Furthermore, the applied service temperature, in the tested range, appears to provide beneficial effect for increasing the fatigue life.

REFERENCES

Beck, L. F. and R. A. Schults, 2009, Seat belt use in states and territories with primary and secondary laws—United States, 2006, J Safety Res. 40, pp. 469–472.

Carpenter, C. S. and M. Stehr, 2008, The effects of mandatory seatbelt laws on seatbelt use, motor vehicle fatalities, and crash-related injuries among youths, J. Health Econ. 27 (3), pp. 642–662.

Chiu, W. T., C. Y. Kuo, C. C. Hung and M. Chen, 2000, The effect of the Taiwan motorcycle helmet use law on head injuries, American Journal of Public Health 90(5) pp.793–796.

Conner, K. A., H. Xiang, G. A. Smith, 2010, The impact of a standard enforcement safety belt law on fatalities and hospital charges in Ohio. J Safety Res 41, pp. 17-23.

Davis, J. W., L. Bennink, K. L. Kaups and S. N. Parks, 2002, Motor vehicle restraints: primary versus secondary enforcement and ethnicity, J. Trauma 52, pp. 225–228.

Dee, T. S. 1998, Reconsidering the effects of seat belt laws and their enforcement status, Accid. Anal. Prev. 30, pp. 1–10.

Dinh-Zarr, T. B., D. A. Sleet, R. A. Shults, S. Zaza, R. W. Elder, J. L. Nichols, R. S. Thompson, D. M. Sosin and the Task Force on Community Preventive Services, 2001, Reviews of evidence regarding interventions to increase the use of safety belts, Am. J. Prev. Med. 21 (Suppl. 4), pp. 48–65.

Eby, D. W., J. M. Vivoda and T. A. Fordyce, 2002, The effects of standard enforcement on Michigan safety belt use, Accid. Anal. Prev. 34, pp. 815–823.

Gorman, D. M., J. C. Huber and S. E. Carozza, 2006, Evaluation of the Texas 0.08 BAC law, Alcohol Alcohol. 41 (2), pp. 193–199.

Homel, R. 1994, Drink-driving law enforcement and the legal blood alcohol limit in New South Wales. Accid. Anal. Prev. 26 (2), pp. 147–155.

Houston D. J. and L. E. Richardson, 2002, Traffic safety and the switch to a primary seat belt law: the California experience, Accid. Anal. Prev. 34 (6), pp. 743–751.

Kim, K., E. Yamashita, 2003, Click it or ticket boosting seat belt use in Hawaii, Transport. Res. Rec. 1830, 18–24.

Kweon, Y. J. 2010, Data-driven reduction targets for a highway safety plan, Transport Polocy 17(4), pp. 230-239.

Leggett, L. M. W. 1997, Using Police Enforcement to Prevent Road Crashes: The Randomised Scheduled Management System. In R. Homel (Ed.), Policing for Prevention: Reducing Crime, Public Intoxication and Injury. Crime Prevention Studies, Vol. 7, pp.175–97. Criminal Justice Press, Monsey, N.Y.

Levine, N. 2006, Houston, Texas, metropolitan traffic safety planning program, Transport. Res. Rec., 1969, 92–100.

Levine, R. S., N. C. Briggs, D. G. Schlundt, N. Stinson, R. C. Warren and I. A. Goldzweig , 2006, Seatbelt law enforcement and motor vehicle crash fatalities among blacks and whites in Louisiana and Mississippi, Southern Medical Journal 99(2), pp. 143-148.

Lund J. and J. E. Aarø, 2004, Accident prevention. Presentation of a model placing emphasis on human, structural and cultural factors, Safety Science 42 (4), pp. 271–324.

Masten, S. V. 2007, Do states upgrading to primary enforcement of safety belt laws experience increased daytime and nighttime belt use? Accid. Anal. Prev. 39(6), pp. 1131-1139.

McCartt, A. T. and V. Shabanova-Northrup, 2004, Factors related to seat belt use among fatally injured teenage drivers, J. Saf. Res. 35, pp. 29–38.

Miles-Doan, R. 1996, Alcohol use among pedestrians and the odds of surviving an injury: evidence from Florida law enforcement data, Accid. Anal. Prev. 28 (1), pp. 23–31.

Newstead, S. V., M. H., Cameron and L.M.W. Leggett, 2001, The crash reduction effectiveness of a network-wide traffic police deployment system, Accid. Anal. Prev. 33, pp. 393–406.

Pande, A., M. Abdel-Aty, and L. Hsia, 2005, Spatio-temporal variation of risk preceding crash occurrence on freeways, Transportation Research Record, 1908, 26–36.

Perkins, B. J., S. D. Helgerson and T. S. Harwell, 2009, Attitudes toward a primary seat belt law among adults in a rural state with a secondary seat belt law, J. Safety Res. **40**, pp. 49–52.

Redelmeier, D. A., R. J. Tibshirani and L. Evans, 2003, Traffic-law enforcement and risk of death from motor-vehicle crashes; case-crossover study, Lancet 361 (9376), pp. 2177–2182.

Retting, R. A. and S. Y. Kyrychenko, 2002, Reductions in injury crashes associated with red light camera enforcement in Oxnard California, American Journal of Public Health 92, pp. 1822–1825.

Rivara, F. P., D. C. Thompson and P. Cummings, 1999, Effectiveness of primary and secondary enforced seat belt laws, Am. J. Prev. Med. 16 (1S), pp. 30–39.

Servadei, F., C. Begliomini, E. Gardini, M. Giustine, F. Taggi and J. Kraus, 2003, Effect of Italy's motorcycle helmet law on traumatic brain injuries, Inj. Prev. 9, pp. 257–260.

Steil, D. A., J. R.Pate, N. A. Kraft, R. K. Smith, B. Dixon, Ding Li and A. Parrish, 2011, Patrol routing expression, execution, evaluation, and engagement, IEEE Transactions on Intelligent Transportation Systems 12(1), pp. 58-72.

Strine, T. W., L. F. Beck, J. Bolen, C. Okoro, S. Dhingra and L. Balluz, 2009, Geographic and sociodemographic variation in self-reported seat belt use in the United States, Accid. Anal. Prev. 42(4), pp. 1066-1071.

Thomas, F. D., R. D. Blomberg, R. C. Peck, L. A. Cosgrove and P. M. Salzberg, 2008, Evaluation of a high visibility enforcement project focused on passenger vehicles interacting with commercial vehicles, J. Safety Res. 39 (5), pp. 459–468.

USDOT 2010, traffic safety facts 2009, US Department of Transportation.

Wagenaar, A. C., M. M. Maldonado-Molina, D. J. Erickson, L. Ma, A. L. Tobler and K. A. Komroa, 2007, General deterrence effects of U.S. statutory DUI fine and jail penalties: long-term follow-up in 32 states, Accid. Anal. Prev. 39(5), pp. 982–994.